*J. Fluid Mech.* (1999), *vol.* 397, *pp.* 171–202. Printed in the United Kingdom

© 1999 Cambridge University Press

# Effect of entrained bubbles on the structure of vortex rings

By G. SRIDHAR AND J. KATZ

Department of Mechanical Engineering, The Johns Hopkins University, Baltimore, MD 21218, USA

(Received 7 May 1996 and in revised form 13 April 1999)

The effect of entrained bubbles on the structure of a vortex ring is studied using particle image velocimetry. Quantitative information on the velocity and vorticity distribution within the vortex core is obtained from multiple images recorded with two 65 frames per second, 35 mm cameras. Bubble trajectories and velocities are also determined from these images. It is demonstrated that for certain combinations of vortex strengths and bubble diameters, a few microscopic bubbles, at very low overall void fraction, shift and macroscopically deform the structure of the vortex. For example, five 512 μm diameter bubbles, entrained by a vortex with core diameter of 2 cm and strength of 160 $cm^2 s^{-1}$, displace the core by 3.5 mm and fragment the core into two regions with peak vorticities that are 20% higher than the original maximum vorticity. The same phenomenon is observed with laminar, transitional and turbulent vortices. Dimensional analysis along with the experimental data show that the distortion is maximum when the bubbles settle, following entrainment by the vortex, in a region located between 20% and 40% of core radius. The governing dimensionless parameters and trends are identified and discussed. The vortex distortions are explained in terms of changes to the liquid momentum caused by the entrainment of the bubbles. It is argued and proven in detail in Appendix A that the change to the liquid momentum due to the presence of the bubble is equal to the bubble volume multiplied by the local stresses that exist in the absence of the bubble. These stresses include the gravity-induced (buoyancy) and hydrodynamic pressure gradients as well as viscous stresses. The buoyancy displaces the core of the vortex upward whereas the force due to hydrodynamic pressure gradients reduces the core size and as a result increases the vorticity. Estimated distortions agree with the experimental data.

## 1. Introduction

### 1.1. *Motivation and rationale*

In a previous work, we studied the motion of bubbles with diameters of less than 1 mm during entrainment by a vortex ring (Sridhar & Katz 1995) and measured the forces acting on them. The buoyancy was determined from the bubble size, which was measured at high magnification using holography. Triple-exposure, high-resolution particle image velocimetry (PIV) images (see the sample in figure 1) allowed measurements of the velocity and acceleration of both the liquid and the bubbles, from which the pressure gradients and the inertia were estimated assuming an added mass coefficient of 0.5. This assumption did not introduce a major error since the inertia was small. Using Stokes flow expressions it was also shown that the Bassett force was negligible. As shown in figure 1, the inertia, buoyancy and forces due to the

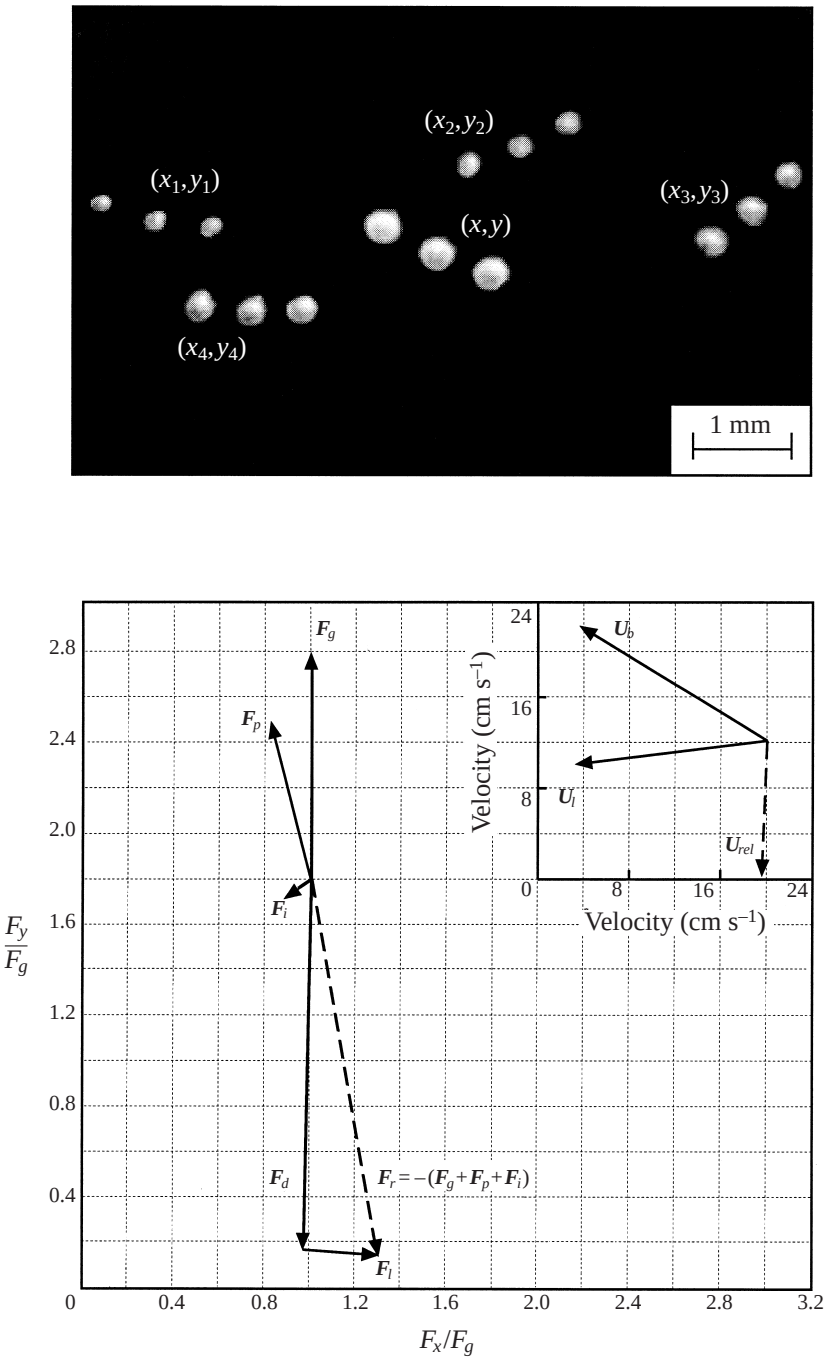


FIGURE 1. Part of a triple exposure PIV image containing a 710 μm bubble at $(x, y)$ surrounded by four 20 μm neutrally buoyant particles located at $(x_i, y_i)$. Also shown are the corresponding vector diagrams of velocities and forces on this bubble (Sridhar & Katz 1995). The subscripts *b, p, i, d, l* in the force balance refer to buoyancy, hydrodynamic pressure, inertia, drag and lift, respectively.

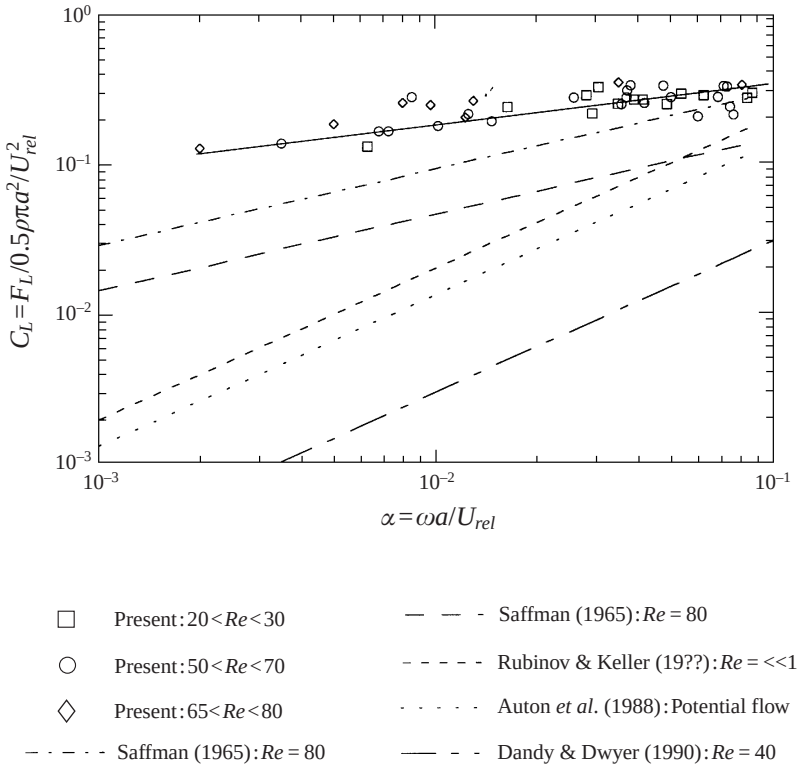


FIGURE 2. The experimental lift coefficients and results of theoretical and numerical models.

hydrodynamic pressure were then balanced with the bubble drag and lift. The drag was parallel to the relative velocity and the lift was normal to it. The results were used for estimating the drag and lift coefficients as well as their dependence on the Reynolds number and local vorticity.

The drag coefficients were found to be very close to that of a solid sphere, indicating that the bubble surface was contaminated. The results for the lift coefficient are plotted in figure 2 along with other theoretical predictions. As addressed in detail in the previous paper, the primary reasons for the discrepancies are simplifying assumptions and differences in the corresponding boundary conditions. For example, Saffman's (1965) expression for the lift coefficient is derived for Stokes flow, in Dandy & Dwyer (1990) a particle is held rigidly, and in Auton, Hunt & Prud'homme (1988) the analysis is based on potential flows. Consequently the estimated lift forces are different. These results agree with Naciri (1992), which to the best of our knowledge is the only other source of experimental data on lift coefficients on bubbles. Bubble trajectories predicted using these lift and drag coefficients substituted in the equation of motion for the bubble,

$$\frac{\mathrm{d}\boldsymbol{U}_b}{\mathrm{d}t} = -2\boldsymbol{g} + 3\left\{\frac{\partial \boldsymbol{U}}{\partial t} + (\boldsymbol{U}\cdot\nabla)\boldsymbol{U}\right\} + \frac{3}{4a}C_d|\boldsymbol{U}_{rel}|\boldsymbol{U}_{rel} + \frac{3}{4a}C_l|\boldsymbol{U}_{rel}|^2\frac{\boldsymbol{U}_{rel}\times\boldsymbol{\omega}}{|\boldsymbol{U}_{rel}||\boldsymbol{\omega}|}, \quad (1a)$$

$$C_d = \frac{24}{Re}(1 + 0.125Re^{0.72}), \quad C_l = 0.47(\alpha)^{0.25}, \quad Re = \frac{2|U_{rel}|a}{\nu}, \quad \alpha = \frac{a\omega}{|U_{rel}|}, \quad (1b)$$

compared very well with the experimental data. Equation (1*a*) is based on the

expression derived by Maxey & Riley (1983), and $\boldsymbol{U}_b$, $\boldsymbol{g}$, $\boldsymbol{U}$, $\boldsymbol{U}_{rel}$, $a$, $\omega$, $\nu$, $C_d$, $C_l$ are the bubble velocity, gravity, fluid velocity, relative velocity of the bubble, bubble radius, local vorticity, kinematic viscosity, drag coefficient and the lift coefficient, respectively. This equation incorporates the effects of inertia (assuming a virtual mass coefficient of 0.5), gravity, lift, drag and local pressure gradients. The Basset force was neglected after estimating its magnitude and showing that it was negligible in our test conditions.

The next question is to what extent do bubbles affect the surrounding fluid? It is already well established that bubbles rising in a quiescent fluid induce liquid motion (Bessler & Littman 1987; Bhaga & Weber 1981; Fan & Tsuchiya 1990; Katz & Meneveau 1996). In the present paper, we study the impact of this bubble-induced motion on the structure of vortex rings. The rings are around 12 cm in diameter and their strengths vary from 100 to 500 $\mathrm{cm^2\,s^{-1}}$. Bubble diameters range from 250 to 750 μm. We will show that under certain conditions even a few entrained bubbles at very low void fractions shift, elongate and distort the core of laminar, transitional and turbulent vortices. For sample photographs that illustrate the extent of vortex deformation, see figure 11(*a–g*). Here the vortex core diameter is about 2 cm and the bubble diameter is 484 μm. Detailed information about the experimental conditions in these figures, along with other examples, is given in §§ 2 and 3. Quantitative data presented in § 3 also indicate that during this process the vortex core is displaced upwards by several bubble diameters and the vorticity distribution within the core is fragmented into smaller structures with higher peak vorticity.

### 1.2. *General background*

There are limited experimental and numerical results on the two-way interactions between bubbles and vortex structures. Research in this field has primarily focused on studies with solid particles as the dispersed phase (Eaton 1994; Hetsroni 1993; Elgobashi & Truesdell 1993; Crowe 1991; Gore & Crowe 1989; Fleckhaus, Hishida & Maeda 1987). The specific gravity of the dispersed phase plays an important role in determining its effect on the liquid phase since heavy particles tend to centrifuge away from the centre of a vortex while buoyant particles are entrained into the core. Consequently, the effect of bubbles on a vortex cannot be directly inferred from the results with heavy particles.

Loth & Cybrinzski (1994) experimentally studied the effect of large bubbles (diameter $> 1$ mm) on the thickness of shear layers. The test flow field was a planar mixing layer with a uniform dilute bubble concentration across the high-speed side. They found that bubbles increased or decreased the shear layer thickness depending on the experimental condition. The decrease in thickness was qualitatively associated with increased eddy and braid coherence whereas the increase in thickness was linked to bubble wake excitation of the flow. Rightley & Lasheras (1995) experimentally analysed bubble dispersion and interphase coupling in a free shear layer. Particular emphasis was given to the energy budget of the flow field resulting from the interaction between the bubble cloud and the large-scale structures dominating the mixing region. They found the energy redistribution in the carrier fluid to be very inhomogeneous with asymmetric peaks. This asymmetry was partly due to the influence of the void fraction field. Both papers clearly indicate that bubbles do have a significant effect on the carrier flow field. The present paper sheds further light on this problem by studying the effect of bubbles on the underlying structure of a vortex.

Taeibi-Rahni, Loth & Tryggvason (1994) studied the interaction between a large cylindrical bubble and a two-dimensional free shear layer by direct simulations of

the full Navier–Stokes equations. They found that the entrained bubble affected the flow when it escaped and cut through the eddy. Buoyancy and centripetal effects were responsible for the interactions, which typically resulted in reduced eddy coherence and size. The unsteady bubble wake caused an increase in velocity fluctuation levels. In this particular problem, the length scale of the dispersed phase and continuous phase were comparable. Keeping in mind that the present bubble diameter is only about 2% of the core size, DNS will encounter difficulties in resolving both the macroscopic flow and the details of the flow structure around individual bubbles, but such information is required if one wishes to explain the phenomena presented later in the paper (see for example figure 11).

Ruetsch & Meiburg (1994) analysed numerically the evolution of a temporally growing two-dimensional shear layer, seeded with a dilute concentration of bubbles. Though their simulated flow was close to the present experimental conditions, their bubble concentrations were large and as a result a continuum approximation was used for the force applied by the bubbles on the liquid. The motion of the continuous phase was modelled with a single-phase-fluid Navier–Stokes equation, which in addition to the usual terms, included a source terms for momentum transport caused by the dispersed phase. In their model the source term was equal to the buoyancy force of the bubbles. The motion of the dispersed phase was obtained by integrating the Lagrangian equation of bubble motion. They observed that bubbles concentrated at equilibrium locations that depended on the bubble size and vortex strength. However, contrary to the present measurements, the accumulation of bubbles was found to reduce the vorticity and pressure gradients near the vortex centre. This disagreement is partly due to differences in flow conditions (e.g. bubble concentrations), but also in part because they neglect the effect of hydrodynamic pressure gradients in the vicinity of the bubble on the momentum introduced by the bubble into the fluid. This issue is discussed further in § 4 of this paper.

## 2. Experimental set-up and measurement techniques

### 2.1. *Test facility and vortex generator*

As shown in figure 3, the experiments are performed in a $0.69\,\mathrm{m} \times 0.76\,\mathrm{m} \times 1.98\,\mathrm{m}$ water tank with windows on all sides for illumination and flow visualization. Vortex rings are generated by discharging a fixed volume of fluid with a piston–cylinder arrangement. The wall of the cylinder is $\frac{1}{4}$ in. thick and the edge of the cylinder, where the vortex ring is formed, is bevelled at 30° to ensure a smooth roll-up of the shear layer. At the end of a stroke the piston comes to rest flush with the end of the cylinder. The strength and structure of a ring generated with this method depends on the orifice geometry, length of the discharged slug and the velocity of the piston (Didden 1979; Glezer 1988). All experiments are conducted with the same cylinder diameter (0.1 m) and slug length (0.1 m). Rings generated by this system are typically 12 cm in diameter, with circulation ranging from 100 to $500\,\mathrm{cm^2\,s^{-1}}$ (determined from PIV data). The convection speeds of the rings vary from 6 to $15\,\mathrm{cm\,s^{-1}}$.

A rodless pneumatic actuator (figure 3) controls the motion of the piston. The maximum stroke length is 0.5 m, and the peak speed is $2\,\mathrm{m\,s^{-1}}$. Two solenoid valves regulate the air pressure to the actuator (up to 690 KPa). The actuator is initially restrained by an electromagnet to help synchronize its motion with the operation of other instruments. The displacement of the piston is recorded using a linear potentiometric sensor. The analog output is acquired with a PC-based data acquisition

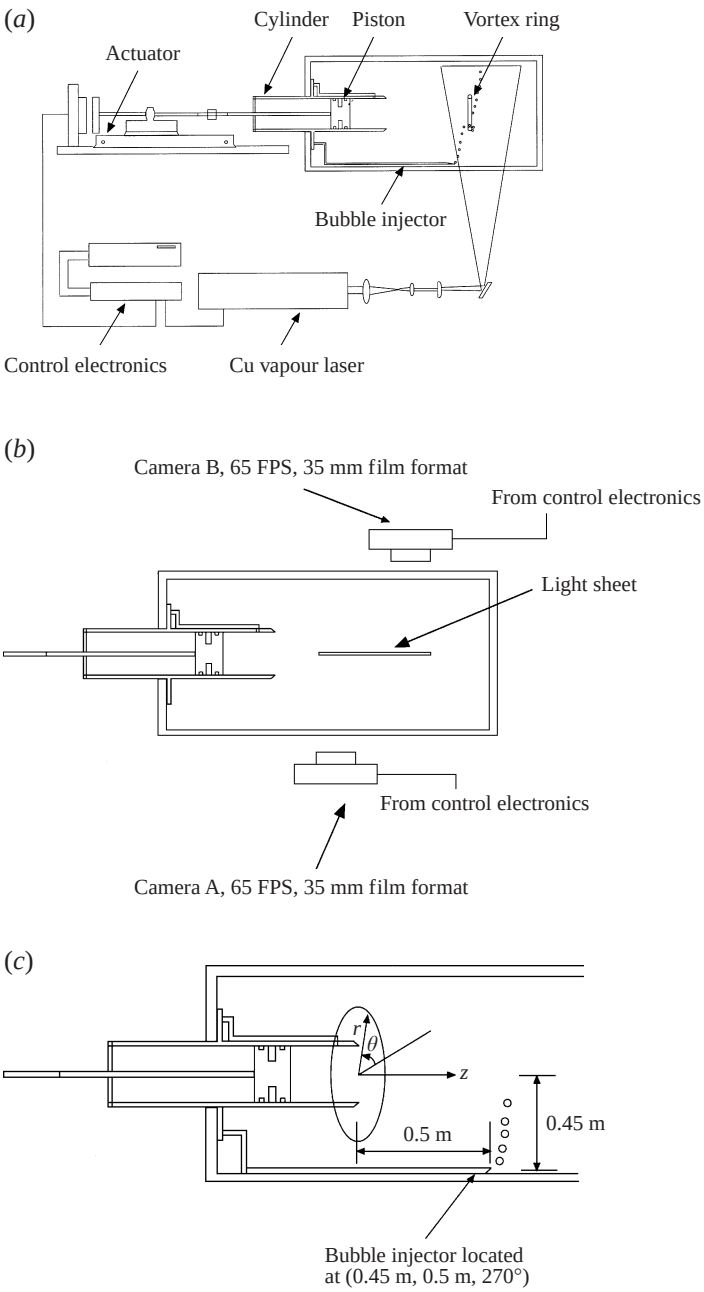


FIGURE 3. (*a*) The experimental set-up. (*b*) Plan view of the vortex chamber identifying the location of cameras A and B. (*c*) The vortex chamber with a reference coordinate system.

system. Figure 4(*a*) is a typical profile of the piston displacement. The data are smoothed and differentiated to obtain the velocity profile of the piston (figure 4*b*).

The strength of a vortex ring generated by this arrangement can be estimated by the cylindrical slug model (Glezer 1988). Here the vortex is modelled as a cylindrical volume of fluid of fixed length, $L_0$, and diameter, $D_0$, moving at a velocity $U_0(t)$ for a

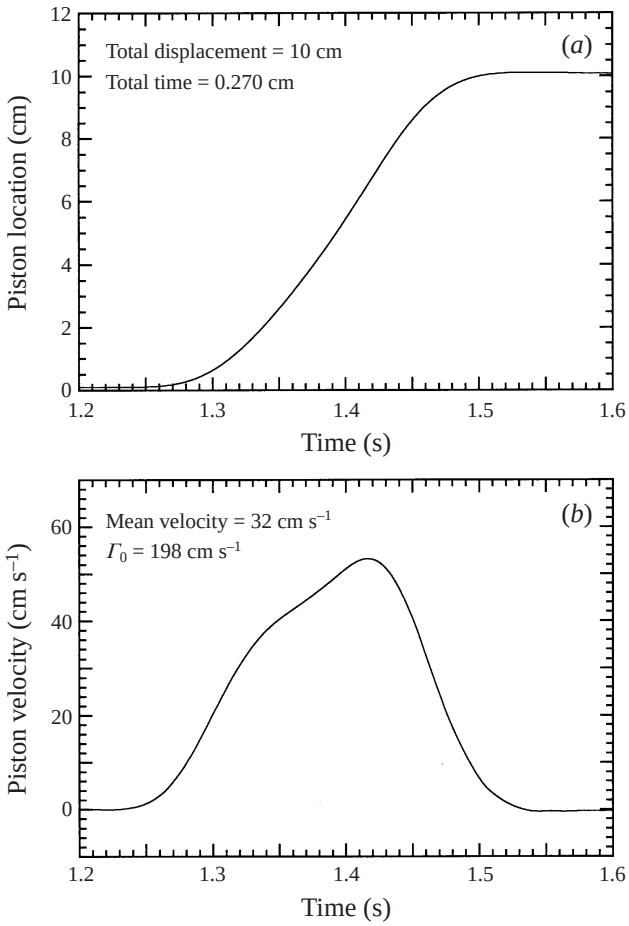


FIGURE 4. (*a*) Typical piston displacement and (*b*) velocity profiles of the vortex generator.

time $T$. The initial circulation of the ring is given by

$$\Gamma_0 = \int_0^T \frac{U_0^2(t)}{2}\,\mathrm{d}t. \tag{2}$$

In figure 5, the actual strength of a vortex ring, $\Gamma$, measured using PIV, is compared to its strength estimated using equation (2). Measurements are performed five ring diameters downstream of the tip of the cylinder. In agreement with Didden (1979) and Glezer (1988), the measured circulation is typically 35% larger than $\Gamma_0$.

The transition of laminar vortex rings into turbulence has been studied experimentally by many researchers including Glezer (1988), Didden (1979), Maxworthy (1974, 1977) and Sallet & Widmayer (1974). From a dimensional analysis of the generating conditions, Glezer (1988) identified the conditions that lead to the generation of laminar and turbulent rings (figure 6). The four points plotted in this figure define the range of vortex rings studied in the present experiments. Images of rings corresponding to these four conditions are provided in figure 7(*a–d*). These images are generated by seeding the interior of the vortex ring generator (only) with fluorescent particles and illuminating a vertical section of the ring with a continuous laser sheet. The exposure time of these extended exposure images is 33 ms (further details on the

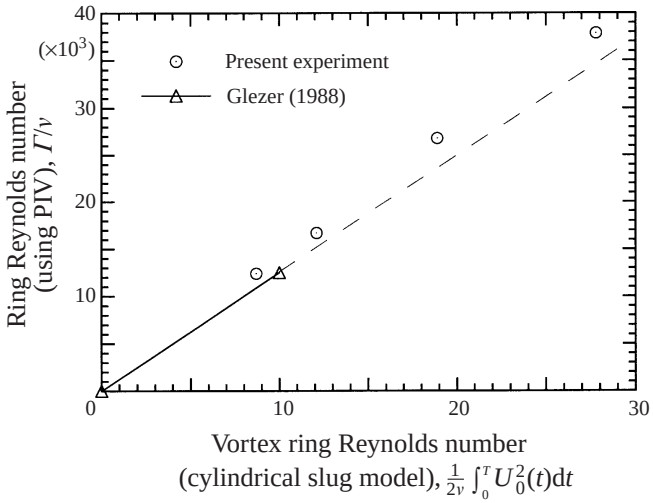


FIGURE 5. Comparison of vortex ring strengths computed using a cylindrical slug model and measured using PIV. The dashed line is extrapolated from figure 4(*b*) of Glezer (1988).

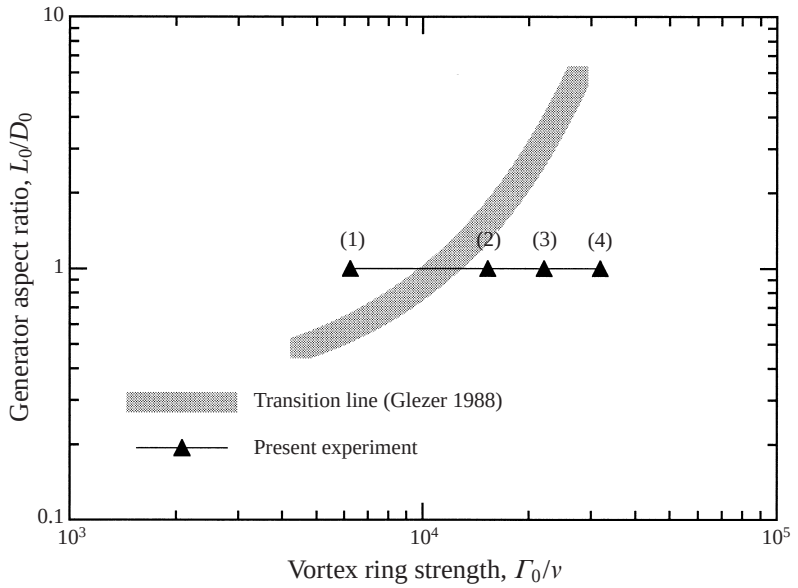


FIGURE 6. The strength of four vortex rings that cover the range of conditions studied during the present experiments. The transition line is reproduced from figure 7 of Glezer (1988). Images of the vortex rings corresponding to the data points 1, 2, 3 and 4 are presented in figure 7(*a–d*).

seeding, laser and optical set-up are provided in the following section). It is evident from the extent of mixing in the near wakes that the ring in figure 7(*a*) is laminar while that in figure 7(*d*) is already turbulent.

In the present experiment, bubbles are injected in a uniform train, 0.5 m downstream of the tip of the cylinder. Following the cylindrical coordinate system shown in figure 3(*c*), the location of bubble injection is at $r = 0.45$ m, $\theta = 270°$, $z = 0.5$ m. Thus, the bubbles are introduced only at the plane of symmetry below the ring and as a result remain in the same plane during the early stages of the entrainment process.

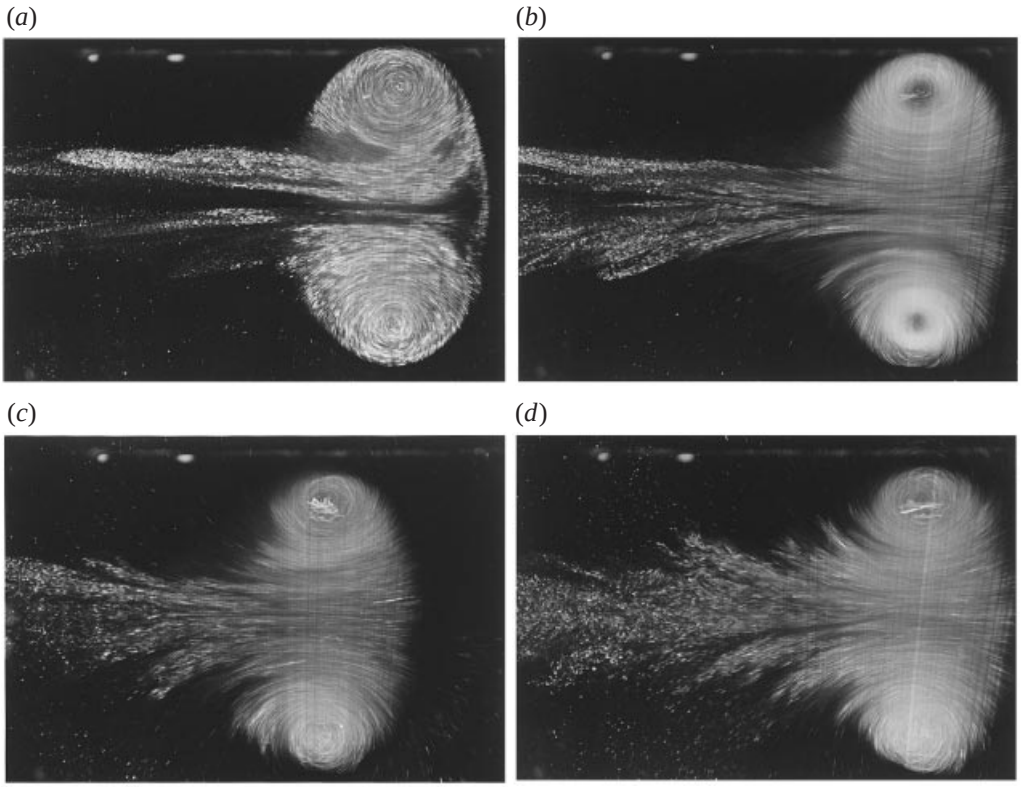


FIGURE 7 (*a–d*). Images of vortex rings corresponding respectively to data points 1, 2, 3 and 4 in figure 6.

After entrainment, when the bubbles distort the core of the vortex and disturb the symmetry of the flow, they migrate out of the plane and travel azimuthally along the torroidal core of the vortex from $\theta = 270^\circ$ to $\theta = 90^\circ$. We refer to this process of bubbles leaving their original plane of injection and migration along the core as a 'bubble escape', though in reality the bubble remains within the vortex at a different azimuthal location.

The bubble injection system consists of a regulator, an air filter, a fine metering valve and a glass injector. The latter is made by stretching a glass capillary tube under heat (Ran & Katz 1991). The tips of the injectors are usually sealed as a result of the stretching and are later etched with hydrofluoric acid until the external diameter of the nozzle is around 10 μm. The bubble size and injection rate are controlled by varying the injector diameter and air pressure. The diameters of the bubbles are measured by recording holograms (Ran & Katz 1991) and high-magnification silhouette images of the bubble train. Since the bubbles are released into a quiescent flow, their size is governed by the buoyancy force, the surface tension force at the bubble–injector interface and the stability of the surface of the bubble. Consequently, the bubble diameter is many times larger than the injector diameter.

### 2.2. *Bubble and liquid velocity measurements*

Quantitative information on the velocity and vorticity distributions within the vortex core is obtained using PIV. Detailed background on PIV can be found in Adrian (1991). Bubble trajectories and velocities are also determined from the same images.

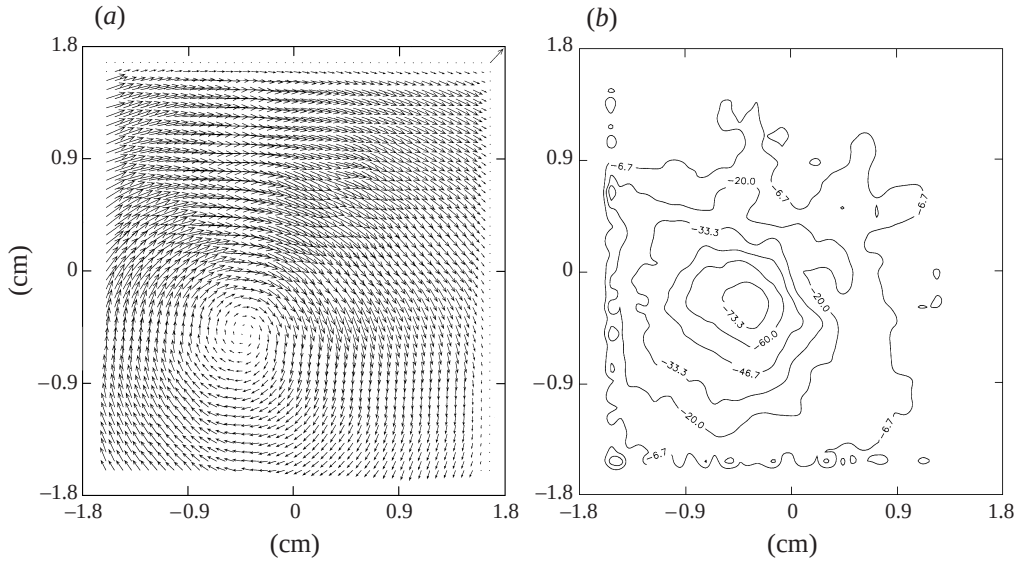


FIGURE 8. (*a*) Characteristic velocity map of an undistorted vortex. The reference vector in the upper right-hand corner of the picture has a horizontal and vertical component of 15 cm s$^{-1}$. (*b*) Vorticity map obtained by computing the velocity gradients from the vector map presented in (*a*). Contours are in steps of $-13.35\,\mathrm{s}^{-1}$.

For this purpose, the flow field is seeded with microscopic (20–30 μm in diameter), neutrally buoyant particles (specific gravity between 0.95 and 1.05) containing fluorescent dye. When illuminated with a copper vapour laser, the dye in the particles fluoresces at 573 nm, i.e. in the yellow range, while the bubbles scatter the incident light (512 nm) and appear green. This difference in colour enables us to distinguish the two phases (Sridhar, Ran & Katz 1991). Automated computation of the velocity field of the ring is not complicated by the presence of the bubbles since the area void fraction is very low, $\sim 10^{-3}$ (when defined as the area occupied by the bubbles divided by the area of the vortex core), and there are no large voids in the liquid flow field.

The Cu vapour laser is pulsed at 300 Hz (the pulse width is $\sim 40$ ns), and images are recorded with two 65 frames per second, 35 mm, Hulcher cameras (figure 3). A typical run provides about 60 frames of useful data. The laser pulses and camera speed are adjusted so that each frame is exposed at least three times. The negative is digitized at a resolution of $3072 \times 2048$ pixels using a Nikon LS3500 slide scanner. The velocity field within the vortex ring is determined using the 'auto-correlation technique', described by Dong, Chu & Katz (1992). Additional error analysis is dealt with in Roth, Hart & Katz (1995). The vorticity distribution is calculated from the spatial velocity gradients as

$$\omega(i,j) = \frac{1}{2}\frac{v(i+1,j) - v(i-1,j)}{\Delta x} - \frac{u(i,j+1) - u(i,j-1)}{\Delta y}, \tag{3}$$

where $u$ and $v$ are the horizontal and vertical velocity components, $i$, $j$ are the horizontal and vertical indices and $\Delta x$, $\Delta y$ are the horizontal and vertical dimensions of the grid. Sample velocity and vorticity maps of a vortex ring obtained by this technique are presented in figures 8(*a*), and 8(*b*) respectively. As discussed in Appendix B, which contains a brief error analysis, the uncertainty in the velocity and vorticity field measurements is about 1% and 10%, respectively.

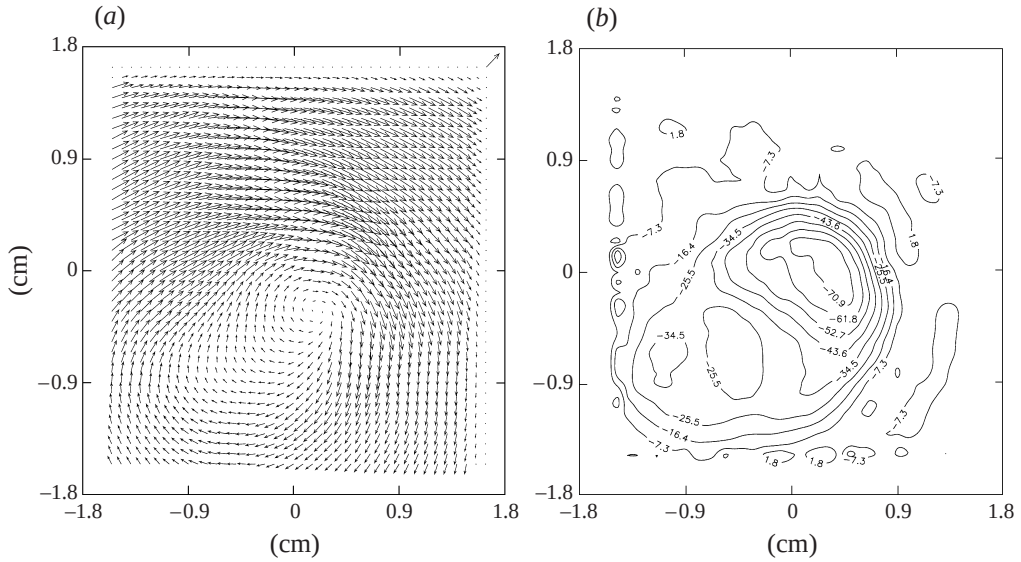


FIGURE 9. (*a*) A typical velocity map of the core of a distorted vortex ring. The reference vector in the upper right-hand corner of the picture has a horizontal and vertical component of 15 cm s$^{-1}$. (*b*) Vorticity map of a distorted vortex ring corresponding to the velocity field presented in (*a*). Contours are in steps of 9.1 s$^{-1}$.

The accuracy of the above procedure is significantly reduced when measuring the velocity fields of distorted vortices. The large velocity gradients within the cores result in significant variations in the displacement between particle pairs within each interrogation window. In such situations, we use a 'particle tracking' technique to compute the local velocity field. Here, individual particle displacements are determined by matching traces of the same particle and measuring the distance between them. The velocity at the location of the particle is determined from the timing of the laser pulses. The randomly distributed velocity vectors are mapped onto a regular grid using a bilinear interpolation scheme (Sridhar & Katz 1995) from which the vorticity field is computed. Figures 9(*a*) and 9(*b*) are typical velocity and vorticity plots of a distorted vortex ring obtained using this technique. The uncertainty in fluid velocity and vorticity measured using this technique is about 0.9% and 10%, respectively (see Appendix B).

## 3. Experimental results

### 3.1. *The process of entrainment, vortex deformation and bubble escape*

At the beginning of each experiment a test run is performed to verify that the vortex core does not distort in the absence of bubbles. Figures 10(*a*) and 10(*b*) are typical images of one such experiment with a laminar vortex ring recorded 450 ms apart. It is clear that the core of the vortex remains intact in the absence of bubbles and that the particle traces follow a nearly circular path around the core centre.

The experiments are then repeated with bubbles in the path of the rings. Figures 11(*a*)–11(*f*) are a time series of images of one such experiment with an initially laminar vortex ring in the presence of 484 μm bubbles. Notice that at the start of this run (figure *a*), the vortex core is intact. The bubble injector is located to the right of the vortex and a few rising bubbles are visible at the lower right-hand corner of

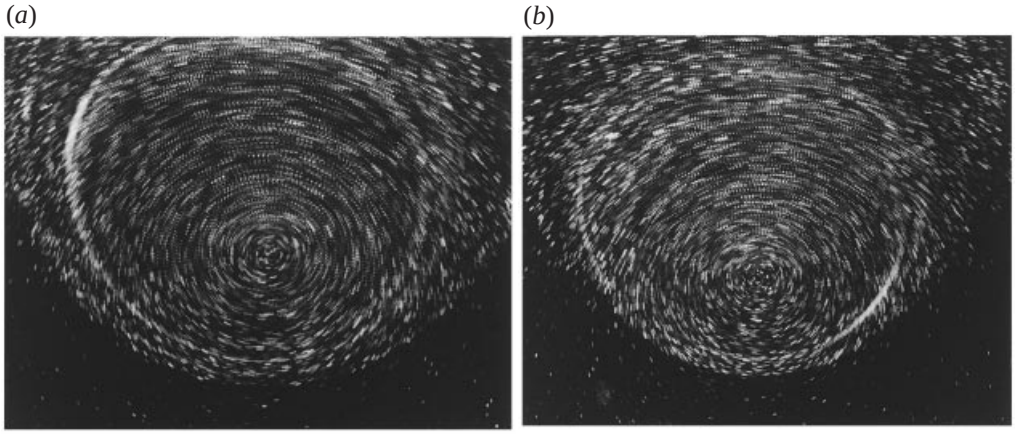


FIGURE 10 (*a*, *b*). Typical images of a laminar vortex ring recorded 450 ms apart, when no bubbles are entrained. The flow is from left to right and images are recorded with Camera A.

this image. As the ring passes through the cloud, it entrains bubbles, which are the bright traces in the centre of the remaining images (figure 11*b*–*f*). Along with bubble entrainment, the vortex core becomes progressively distorted. Qualitatively, the core appears to be elongated and inclined at about 45° to the horizontal. The particle traces now appear to be following an elliptical path around the vortex 'centre' (note that the point of zero velocity is not the centre of vorticity) with the bubbles located close the upper right-hand corner of the ellipse. The distortion is maximum at 321 ms (figure 11*c*) when the vortex centre seems to break into two distinct structures. Such multiple structures are also evident from figure 9. At subsequent times, apparently due to the vortex distortion, the bubbles leave the plane of the laser sheet and migrate azimuthally along the core of the ring. This 'escape' and migration process cannot be seen directly in the samples, but can be observed visually during the experiments. As the bubbles begin to escape, when they are only slightly out of focus, they appear as smudges in figures 11(*e*) and 11(*f*). As the number of bubbles in the core decreases the core distortions become weaker. Eventually, at 677 ms (figure 11*g*), the core regains its original shape.

A similar process of bubble entrainment, vortex distortion, bubble escape, and the vortex returning to its original shape is also observed with transitional and turbulent vortex rings, provided that the 'appropriate' (see § 4.2) number and sizes of bubbles are entrained. Figure 12 is a sample image of a transitional ring with a ring Reynolds number $\Gamma = 170\,\mathrm{cm^2\,s^{-1}}$ entraining 512 μm bubbles. Figure 13 is an image of a typical turbulent ring with $\Gamma = 330\,\mathrm{cm^2\,s^{-1}}$ entraining 1100 μm bubbles. In both cases, the elongation and orientation of the core are qualitatively similar to that in figure 11(*c*) (the opposite directions are a result of using a camera located on the other side of the test facility).

Quantitative data on the entrainment, deformation, bubble escape and return to the original shape can be obtained from the vorticity plots of the vortex rings. A sample vorticity plot of an undistorted vortex ring containing mostly concentric contours is provided in figure 8(*b*). In the absence of bubbles, the vortex simply translates horizontally at a constant velocity and the vorticity distribution remains essentially the same. A time sequence of vorticity plots of a similar vortex ring as it entrains bubbles is presented in figure 14(*a*–*g*). The mean vortex strength is $160\,\mathrm{cm^2\,s^{-1}}$ and it

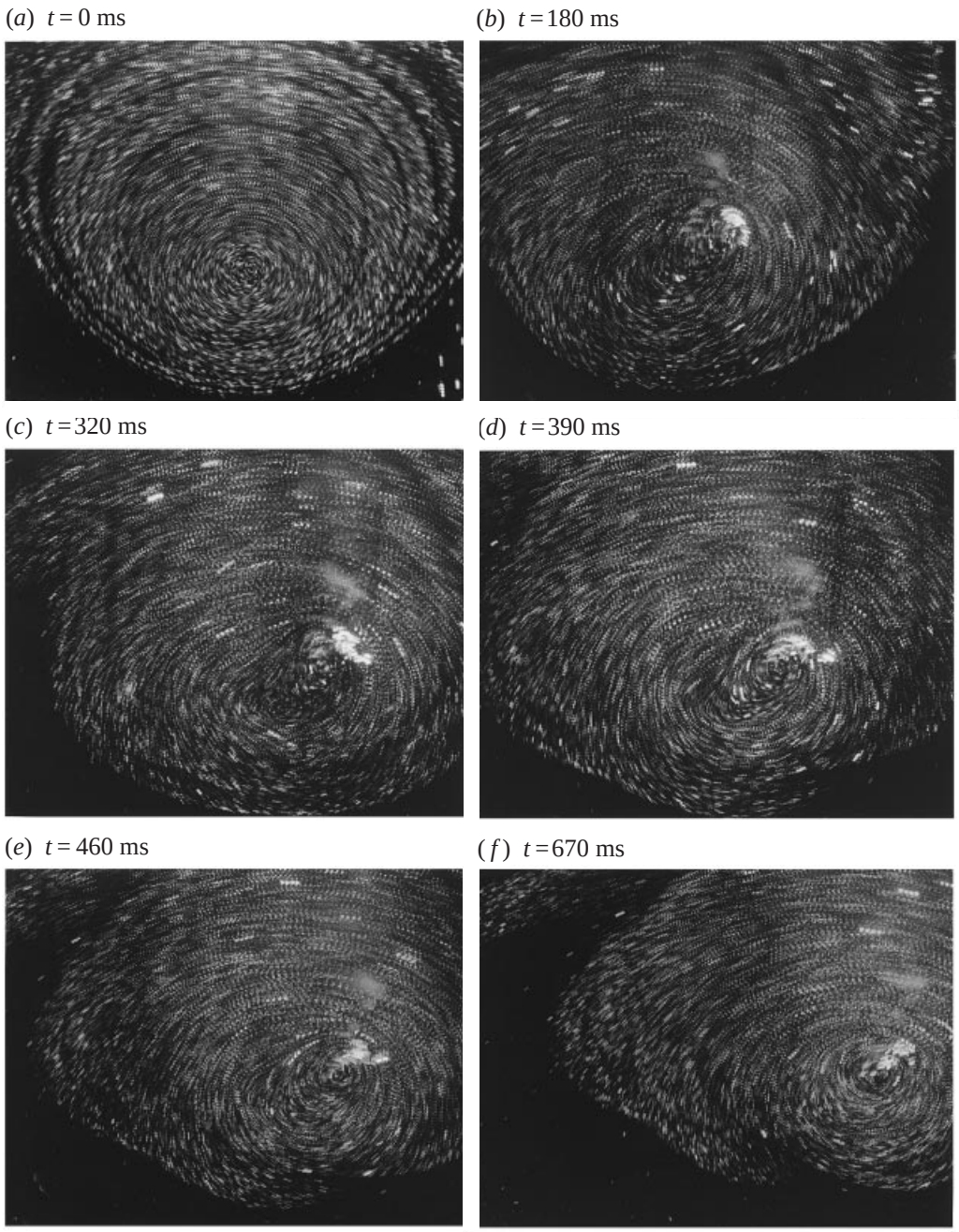


FIGURE 11 (*a–f*). Successive images of a laminar vortex ring as it entrains 484 μm bubbles. The vortex ring is moving from left to right and images are recorded with Camera A.

entrains 512 μm diameter bubbles, whose locations in the vortex are indicated by solid circles. (Note that the circle diameter is not indicative of the bubble size.) Initially, there are no entrained bubbles in the vortex and the core appears as a single structure (figure 14*a*). The total strength of the ring is $126\,\mathrm{cm}^2\,\mathrm{s}^{-1}$ with a peak vorticity of $87\,\mathrm{s}^{-1}$. At this time, only part of the vortex core is in the camera field of view, which

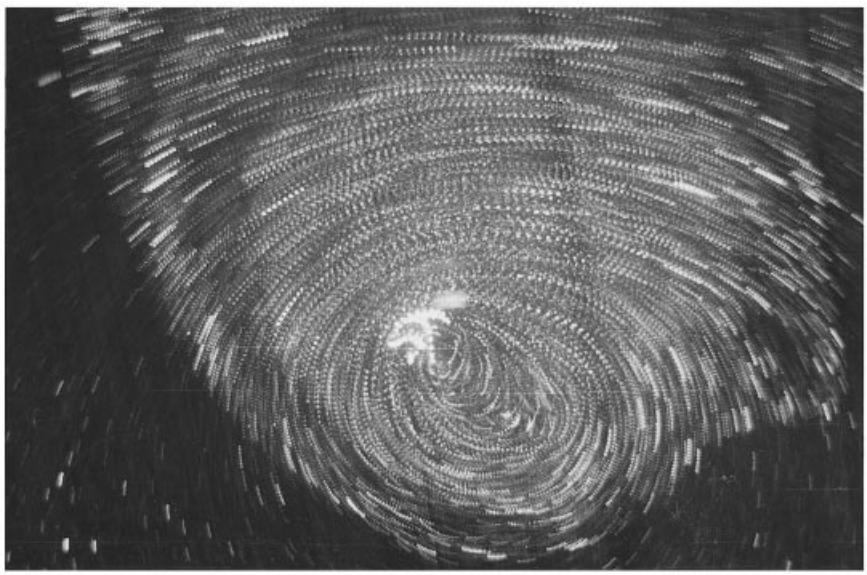

FIGURE 12. Image of an initially circular, transitional vortex ring (see figure 6) after entraining 512 μm bubbles. The flow is from right to left as the image was recorded with Camera B.

FIGURE 13. Image of an initially circular turbulent vortex ring after entraining 1100 μm bubbles. The flow is from right to left as the images were recorded with Camera B.

explains the lower circulation. The initial centroid of vorticity of the vortex core in figure 14(*a*) is chosen as the origin of the coordinate system ($X = 0$; $Y = 0$) for this entire sequence. This centroid is defined as

$$X_{cen} = \sum_i X_i \omega_i^2 \Big/ \sum_i \omega_i^2, \qquad Y_{cen} = \sum_i Y_i \omega_i^2 \Big/ \sum_i \omega_i^2, \tag{4}$$

where $\omega_i$ is the local vorticity at $(X_i, Y_i)$. The centroid is weighted with the square of the local vorticity in order to reflect (bias towards) the location of regions of higher vorticity. The centroid in subsequent vorticity maps is indicated by a solid square inscribed in a circle.

At 286 ms (figure 14*b*) the strength of the vortex is $160\,\mathrm{cm^2\,s^{-1}}$. At this time the vorticity distribution begins to distort. With core distortion, the peak vorticity increases by 10% and the centroid is displaced upwards by 0.23 cm. At 477 ms (figure 14*c*), the distortion is more pronounced. The core now consists of two regions of high vorticity with the bubbles located slightly below and between them. The peak vorticity is 12% higher than the initial value and the centroid is further displaced upwards by 0.33 cm.

At 667 ms (figure 14*d*), five bubbles are entrained into the core of the vortex, which is fragmented into two distinct regions. The peak vorticity within these regions is 128% and 116% of the original value while the total circulation remains unchanged, at $156\,\mathrm{cm^2\,s^{-1}}$. Both inclined and elongated structures are significantly displaced from the original centre. The high-vorticity regions are located 0.64 cm and 0.52 cm above the original core location, while the centroid is elevated by 0.33 cm.

In figure 14(*e*), which is a plot of the core at 955 ms, the two regions of high vorticity are horizontal and more diffused. The total strength is still $160\,\mathrm{cm^2\,s^{-1}}$. Here, the bubbles are no longer clustered and are instead located farther away from the centroid. At subsequent times (figures 14*f* and 14*g*), the bubbles leave the plane of the light sheet and escape by rising along the core of the ring. The regions of high vorticity then coalesce (figure 14*f*) and the vortex eventually regains its original configuration and elevation at 1600 ms (figure 14*g*). At this time only one bubble is left within the core. The overall convection speed of the vortex core remains unchanged during the whole process. Also, following the distortion, the vortex is located in the same region as a vortex with a similar strength that is not seeded by bubbles. These trends indicate that the observed vortex shift and fragmentation is not a result of overall vortex ring instability.

Not all entrained bubbles cause such a major distortion of the core, i.e. displacements of several bubble diameters and fragmentation into secondary structures with 25% higher vorticity. Small bubbles whose final locations after entrainment are 'close' (see § 3.2 for a dimensional analysis) to the centre of the core do not have a noticeable effect on the vortex structure. For example, in figure 15, which is the vorticity map of a turbulent vortex ($\Gamma = 311\,\mathrm{cm^2\,s^{-1}}$) after entraining five 512 μm bubbles, it is evident that the vortex core is not distorted significantly. Here the bubbles simply remain within the core for the duration of the experiment ($\sim 500$ ms). In addition, 'large' bubbles (see the discussion in § 3.2) whose location following entrainment is 'far' from the core also have little effect on the vorticity distribution (see § 3.2).

There are also certain combinations of bubble diameters and vortex strengths where the vortices are 'marginally' affected. Here, 'marginal' means core displacement of less than one bubble diameter, but still distortion with about 10% increase in the peak vorticity. Figure 16 is an example of such an interaction, where a ring with $\Gamma = 192\,\mathrm{cm^2\,s^{-1}}$ entrains four 1100 μm bubbles. Here too the entrainment and distortion process is similar to that described in figure 14(*a–g*) but the distortions are less severe. In the results and discussion that follow in § 3.2, the test conditions of the present experiment are classified into these three groups, i.e. severe, marginal and no distortion of the core. We will show that the important parameter governing the extent of core deformation is the location of the bubble after entrainment. This conclusion will be derived from the experimental data and a dimensional analysis of the forces acting on the bubble.

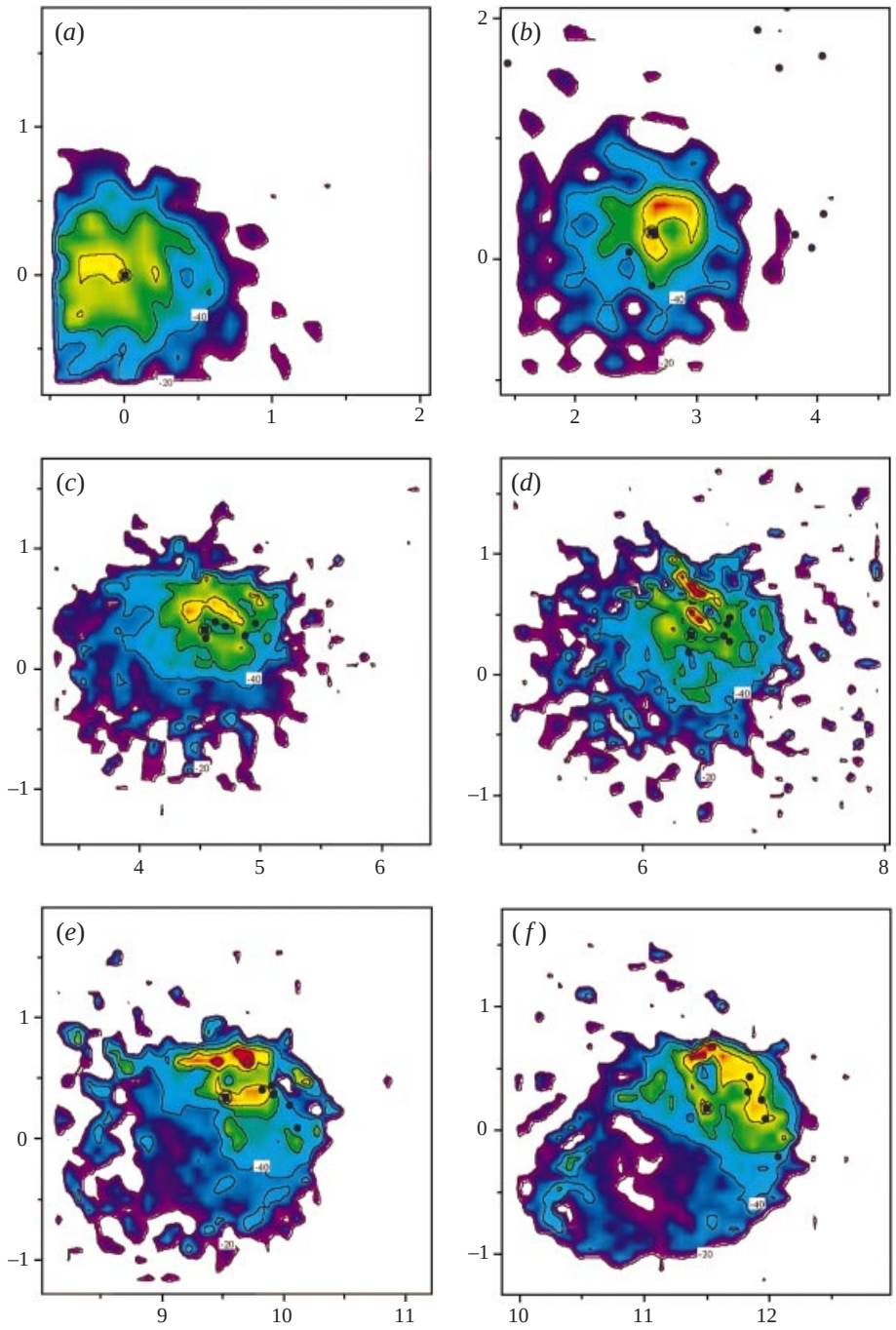


FIGURE 14. For caption see facing page.

### 3.2. *Relationships between bubble size, vortex strength and deformation*

When a bubble is entrained into a vortex, and the core does not deform, the bubble eventually comes to rest relative to the vortex centre. At this location, which we define as the 'final' location of the bubble, the bubble acceleration is zero and it

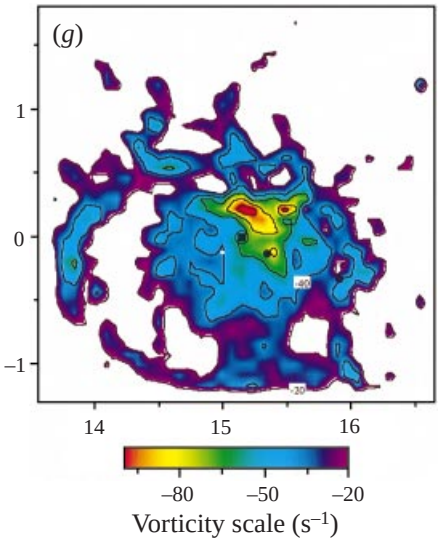


FIGURE 14. Time sequence vorticity plots of the core of a vortex entraining 512 μm bubbles. The location of the centre of the vortex at time $t = 0$ ms is at $(x, y) = (0, 0)$. The location of the centre at subsequent time steps is indicated in subsequent time steps by a square inscribed in a circle. Vorticity contours are in steps of 20 $s^{-1}$. Entrained bubbles are represented by the solid circles. (*a*) Time = 0 ms, $\Gamma = 126$ $cm^2$ $s^{-1}$; (*b*) 286 ms, 160 $cm^2$ $s^{-1}$; (*c*) 477 ms, 164 $cm^2$ $s^{-1}$; (*d*) 667 ms, 156 $cm^2$ $s^{-1}$; (*e*) 955 ms, 160 $cm^2$ $s^{-1}$; (*f*) 1146 ms, 166 $cm^2$ $s^{-1}$; (*g*) 1528 ms, 164 $cm^2$ $s^{-1}$.

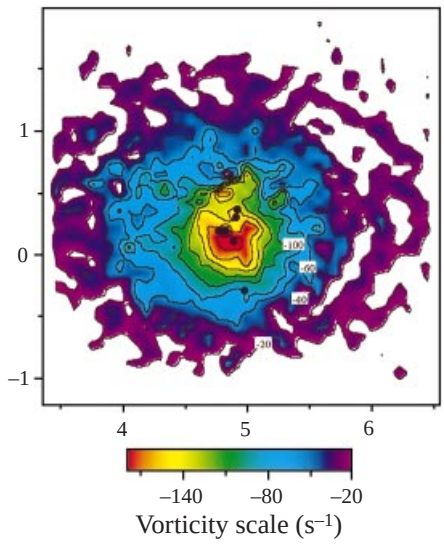


FIGURE 15

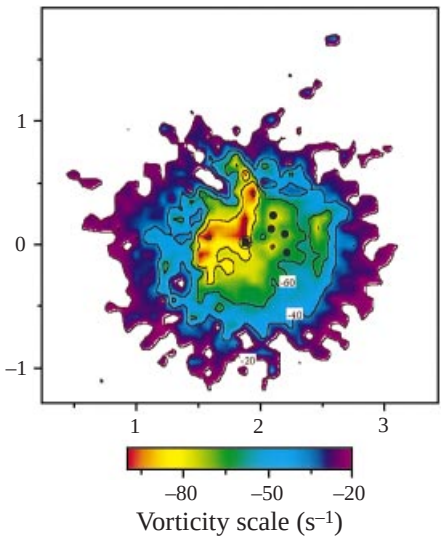


FIGURE 16

FIGURE 15. Example of an unaffected vortex ring after entraining five 512 μm bubbles. Vorticity contours are in steps of 20 $s^{-1}$. Time = 360 ms, $\Gamma = 311$ $cm^2$ $s^{-1}$.

FIGURE 16. Example of a marginally affected vortex ring after entraining four 1100 μm bubbles. Vorticity contours are in steps of 20 $s^{-1}$. Time = 700 ms, $\Gamma = 192$ $cm^2$ $s^{-1}$.

simply translates rectilinearly with the vortex ring. Such horizontal motion is evident, for example, in figure 13. Thus, the equation of motion of the bubble (equation (1*a*)) reduces to

$$0 = -2\boldsymbol{g} + 3\left\{\frac{\mathrm{D}\boldsymbol{U}}{\mathrm{D}t}\right\} + \frac{3}{4a}C_d|\boldsymbol{U}_{rel}|\boldsymbol{U}_{rel} + \frac{3}{4a}C_l|\boldsymbol{U}_{rel}|^2\frac{\boldsymbol{U}_{rel}\times\boldsymbol{\omega}}{|\boldsymbol{U}_{rel}||\boldsymbol{\omega}|}. \tag{5}$$

This equation states that the sum of the forces acting on the bubble, including the pressure gradients due to gravity (buoyancy), drag, lift, hydrodynamic pressure gradients and virtual mass (although the bubble acceleration is zero, the liquid acceleration is not and as a result the virtual mass is equal to 50% of the liquid acceleration). For the purpose of dimensional analysis, let us assume that the bubble comes to rest at a distance $r$ from the centre of a vortex with strength $\Gamma$ and radius $R$, containing a uniform vorticity distribution. Then, an appropriate velocity scale for $\overline{U}_{rel}$ is $\Gamma r/2\pi R^2$ and for the local pressure gradient is $\rho_l r\Gamma^2/4\pi^2R^4$. Equation (5) can now be written in a non-dimensionalized form as

$$\bar{\boldsymbol{g}} = \frac{3}{8\pi^2}\bar{r}\left(\frac{\mathrm{D}\overline{\boldsymbol{U}}}{\mathrm{D}\bar{t}}\right) + \frac{3}{32\pi^2}C_d\frac{\bar{r}^2}{\bar{a}}|\overline{\boldsymbol{U}}_{rel}|\overline{\boldsymbol{U}}_{rel} + \frac{3}{32\pi^2}C_l\frac{\bar{r}^2}{\bar{a}}|\overline{\boldsymbol{U}}_{rel}|^2\frac{\overline{\boldsymbol{U}}_{rel}\times\overline{\boldsymbol{\omega}}}{|\overline{\boldsymbol{U}}_{rel}||\overline{\boldsymbol{\omega}}|}, \tag{6a}$$

$$C_d = f(\bar{a},\bar{r},\Gamma/\nu), \qquad C_l = h(\bar{a},\bar{r},\overline{\omega}), \tag{6b}$$

where

$$\bar{g} = \frac{gR^3}{\Gamma^2}, \quad \bar{r} = \frac{r}{R}, \quad \overline{U} = \frac{U}{\Gamma r/2\pi R^2}, \quad \bar{t} = \frac{2\pi R^2}{\Gamma}, \quad \overline{\omega} = \frac{\omega}{\Gamma/\pi R^2}, \quad a = \frac{a}{R}. \tag{6c}$$

The dimensionless parameters in (6*a*) and (6*b*) are $\bar{r}$, $\bar{a}$, $\bar{g}$ and $\Gamma/\nu$. Of these parameters, $\bar{r}$ is a dependent variable while the other three are independent. Note that $\bar{r}$ is only indirectly dependent on $\Gamma/\nu$ through the drag coefficient. In the present range of Reynolds numbers $20 < Re < 80$, the values of $C_d$ are of the same order of magnitude (it changes from 1.2 to 2.8) and consequently $\bar{r}$ is expected to be weakly dependent on $\Gamma/\nu$. Similarly, the dependence of $C_l$ on $\overline{\omega}$ is also weak (Sridhar & Katz 1995). Thus, the dependence of $C_d$ and $C_l$ on $\Gamma/\nu$ and $\overline{\omega}$ are neglected in the present discussion. The only independent parameters left are $\bar{g}$ and $\bar{a}$. As $R$ is constant in the present study, $\bar{g}$ and $\bar{a}$ can be combined to form a single non-dimensional variable $\bar{g}\bar{a}^3 = ga^3/\Gamma^2$. This term represents the ratio between buoyancy and the force due to the hydrodynamic pressure gradients.

The present test conditions are plotted in figure 17 with $\bar{r}$ and $ga^3/\Gamma^2$ as the two axes. The value of $\bar{r}$ (dimensionless 'final' location) for each experimental condition is determined by solving (6*a*) and (6*b*). Due to its implicit form, we have found that the simplest approach is to position a bubble randomly within the core and follow its trajectory by integrating its equation of motion (1*a*, *b*) until it comes to rest with respect to the vortex centre. The procedures of integration are discussed in Sridhar & Katz (1995) and summarized briefly in § 4 of this paper. The vortex core is assumed to be 1 cm in radius, with uniformly distributed vorticity of $\Gamma/\pi R^2$. $\Gamma$, $R$ and $a$ are based on the experimental data. Notice that all the present test conditions, which are plotted in figure 17, collapse onto a single curve. The slight scatter in the data is due to the weak dependence of $\bar{r}$ on the ring Reynolds number, $\Gamma/\nu$, which is neglected in the dimensional analysis.

The observed extent of vortex deformation, defined based on the three levels introduced before (severe distortion – figure 14, no distortion – figure 15 and marginal distortion – figure 16) are also identified in figure 17. It is evident that bubbles that

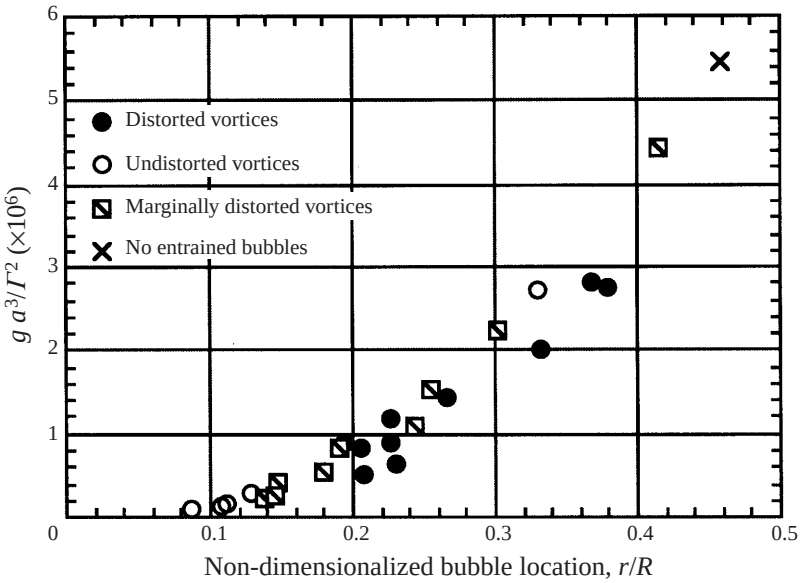


FIGURE 17. The present experimental conditions and extent of vortex distortion.

severely distort and displace the vortex core have final locations that fall in the range $0.2 < \bar{r} < 0.4$. Bubbles located at $\bar{r} < 0.13$ do not cause distortion and for $\bar{r} > 0.45$, $ga^3/\Gamma^2 > 5 \times 10^{-6}$ the bubbles are not entrained by the vortex. In the latter case the gravity is sufficiently high compared to the hydrodynamic pressure gradients that the bubbles escape and as a result do not cause vortex deformation. Regions with strictly marginal distortions are $0.14 < \bar{r} < 0.2$ and $0.4 < \bar{r} < 0.45$, i.e. on both sides of the severe distortion range. However, the marginal distortion cases are scattered over the entire $\bar{r} > 0.13$ range. As will be discussed also in § 4, besides the final location of the bubble the extent of deformation is governed by the number of entrained bubbles and the residence time of the bubbles within the vortex core. Consequently, even if the bubbles are in a size range that is prone to cause severe deformation, too few bubbles or a too short residence time may reduce the extent of distortion. The range prone to distortion is clearly $0.2 < \bar{r} < 0.4$ and it is bounded on both sides with regions prone to marginal distortion.

In order to explain the observed trends, recall that when the bubble reaches its final location the relative velocity $\overline{U}_{rel} = \Gamma r/2\pi R^2$ is proportional to $r$. Thus, the drag and lift forces are proportional to $a^2r^2$ (neglecting Reynolds number effects), whereas the forces due to hydrodynamic pressure gradients and virtual mass are proportional to $a^3r(\mathrm{D}\boldsymbol{U}/\mathrm{D}t = \Gamma^2 r/4\pi^2R^4)$. The buoyancy is obviously proportional to $a^3$. These relationships imply that forces due to buoyancy, pressure gradients and inertia increase more rapidly with $a$ than the lift and drag. Consequently, as the bubble size increases its final location has to move outward, where the quadratic increase of lift and drag with $r$, being faster than the pressure gradients, virtual mass and buoyancy, compensates for the slower increase of lift and drag with $a$. As a result, the final location of a bubble as well as all the forces acting on it increase with bubble size and its final location.

As will be discussed in detail in § 4.1, the forces introduced due to the presence of the bubble, that do not exist in its absence, are the drag, lift and virtual mass. Their

combined effect would result in the formation of a 'wake', or induced liquid motion around the bubble. The magnitude of these forces and as a result their impact on the liquid momentum increases (at varying degrees) with $\bar{r}$. Thus, one should expect that the deformation to the core would increase with increasing bubble radius and final location. This conclusion is consistent with the trends demonstrated figure 17 only for $\bar{r} < 0.4$. Larger bubbles that settle at larger $\bar{r}$ cause less vortex deformation for two reasons. First, although these larger bubbles induce greater liquid motion locally, they are located farther from the core centre and as a result they mostly affect the flow at the perimeter of the vortex. Second, the characteristic residence time of these bubbles in the plane of symmetry at the bottom of the vortex ($\theta = 270°$) is shorter due to the increased likelihood of escape with increasing buoyancy force and being close to edge of the core. In fact, there is no bubble entrainment at $\bar{r} > 0.45$.

## 4. Discussion

The present experimental results demonstrate that a few microscopic bubbles can significantly distort a vortex ring. This phenomenon is quite unexpected and has not been reported earlier. Furthermore, a simple dimensional analysis shows a correlation between the final location of the entrained bubbles and the extent of vortex deformation. Both phenomena can be understood by carefully examining the nature and effect of bubble-induced liquid motions.

### 4.1. *Changes in the liquid momentum due to the presence of bubbles*

The surface forces acting on a bubble are buoyancy (pressure gradients in the liquid resulting from gravity), hydrodynamic pressure (that would exist in the absence of the bubble), added mass, drag (viscous and form), lift and Basset forces (Maxey & Riley 1983). The only body force acting on the bubble is its own weight, which is negligible. Thus, the sum of the surface forces acting on the bubble is zero. A sample balance of these forces is shown in figure 1(*a*). To determine the effect of the bubble on the liquid momentum one needs to identify the effect on the surrounding liquid caused by replacing a body of liquid by a massless sphere. As argued in detail in Appendix A and also recently in Druzhinin & Elgobashi (1998), the motion of a bubble in a flow field changes the liquid momentum (applies a force on the liquid) by $\Delta \boldsymbol{F}^b$, where

$$\Delta \boldsymbol{F}^b = \rho V_B \left( \frac{\mathrm{D}\boldsymbol{U}^0}{\mathrm{D}t} - \boldsymbol{g} \right). \tag{7a}$$

Here $\boldsymbol{U}^0$ is the undisturbed flow field at the location of the bubble that would exist in the absence of the bubble, and $V_B$ is the bubble volume. Note that $(\mathrm{D}\boldsymbol{U}^0/\mathrm{D}t) - \boldsymbol{g}$ is simply the local stress gradients that would exist in the absence of the bubble. On the bubble surface these stress gradients are balanced by the drag, lift, virtual mass and Bassett forces. The last is negligible in the present case as discussed before. Thus, $\Delta \boldsymbol{F}^b$ can also be expressed as

$$\Delta \boldsymbol{F}^b = -\rho V_B \left[ \frac{3}{8a} C_d |\boldsymbol{U}_{rel}| \boldsymbol{U}_{rel} + \frac{3}{8a} C_l |\boldsymbol{U}_{rel}|^2 \frac{\boldsymbol{U}_{rel} \times \boldsymbol{\omega}}{|\boldsymbol{U}_{rel}||\boldsymbol{\omega}|} - \frac{1}{2} \left( \frac{\mathrm{D}\boldsymbol{U}_b}{\mathrm{D}t} - \frac{\mathrm{D}\boldsymbol{U}^0}{\mathrm{D}t} \right) \right]. \tag{7b}$$

In their analysis, Druzhinin & Elgobashi (1998) use expressions for the drag force in Stokes flow and neglect the effect of the lift.

### 4.2. *Effects of bubbles on the location and shape of the vortex core*

In order to estimate the impact of the bubbles on the flow structure within the vortex it is necessary to estimate the buoyancy and pressure gradients along the trajectory of the bubble. The buoyancy is known from the bubble size ($=\frac{4}{3}\pi a^3\rho g$), but the pressure gradients depend on the location of the bubble within the vortex. As shown in the next section, the bubble trajectory can be determined using equation (1*a*, *b*) and the measured lift and drag coefficients. These forces must be inserted in the Navier–Stokes equations for the liquid motion to determine the impact of the bubble on the vortex structure. In the context of this paper, however, we only wish to explain the experimental observation and confirm that the momentum exchange due to the entrainment of a few bubbles can actually cause the observed phenomena. For this purpose we look at a simple vortex prior to deformation and estimate the overall impact of the momentum added by the bubbles. The buoyancy force is always pointing upward, but the force due to the hydrodynamic pressure gradient ($\partial p/\partial r = \rho v_\theta^2/r$) varies in magnitude and direction during the entrainment process.

*Buoyancy effects* Let us first consider the effect of just the buoyancy. During the entrainment process the bubble encircles the centre of the core while continuously introducing momentum into the fluid. Consequently, the effect of the bubble is distributed over the entire core of the vortex. We need to estimate the thickness of the region affected by the bubble, keeping in mind that we deal with a single layer of bubbles affecting a disk of fluid. Assuming a thickness equal to the bubble diameter, $2a = 512\,\mu\text{m}$, the mass of the affected liquid is approximately equal to $2\pi aR^2\rho_l$. The acceleration, $A$, of this fluid mass, due to the momentum introduced by the buoyancy of the five bubbles, is then $A = 5\frac{4}{3}a^3g/2aR^2 = 2.0\,\text{cm s}^{-2}$. Thus, the displacement of the core due to bubble buoyancy, being equal to $\frac{1}{2}At^2$ and $t = 600\,\text{ms}$, is 0.36 cm. Note that the choice of thickness is somewhat arbitrary. In reality the displaced fluid layer should be wider due to the effect of viscosity. For example, if one chooses the width of a wake due to viscous diffusion, $(4\nu t)^{1/2}$, and $t$ as about one half the characteristic entrainment time ($0.5t = 300\,\text{ms}$), the width doubles and the core displacement is halved. However, it is clear from these estimates that the five microscopic bubbles can displace the core by the measured amount.

*Pressure gradient effect* A similar analysis can also be carried out with the momentum introduced by the pressure gradients. As the bubbles spiral around the core, before they reach their 'final location', the added momentum is always directed radially toward the centre of the vortex. Thus, as a crude estimate, there is no net displacement of the core. Instead, the bubbles cause a reduction in the area of the core and as a result, an increase in the local vorticity. When the bubbles reach their final location, above and ahead of the vortex centre, and stop spiralling, the direction of the added momentum becomes steady, but still points towards the centre. In this case the hydrodynamic pressure gradients oppose in part the buoyancy effect.

As discussed in the next subsection, where the experimental trajectories are compared to numerical predictions, the bubbles spiral around the centre during a significant portion of the period before the vortex reaches its maximum deformed state (figure 14*d*). Thus, the discussion focuses first on the effect of a bubble spiralling around the core. The pressure gradient in a Rankine vortex is $\rho_l r\Gamma^2/4\pi^2R^4$. At the 'final location', for which the vortex distortion is maximum, $r/R = 0.3$ (§ 3.2). Using the experimental $\Gamma = 160\,\text{cm}^2\,\text{s}^{-1}$ and $R = 1\,\text{cm}$ (figure 14), the pressure gradient is $195\,\text{dyne cm}^{-3}$, i.e. about one fifth of the gravity-induced pressure gradients. For the

same disk of liquid discussed before, whose width is equal to the bubble diameter, the spatially and temporally averaged acceleration towards the vortex centre is about $0.4\,\mathrm{cm^2\,s^{-1}}$. Thus, in 600 ms the radius of the core would be reduced by 0.07 cm, from 1 cm to 0.93 cm (causing out of plane motion). This radial acceleration would then cause a 14% reduction in the core area, increasing the average vorticity by almost 16%. This estimate is consistent with the level of increase in the experimental peak vorticity. However, one should be careful in interpreting this agreement since the estimates here are crude and refer to the mean vorticity. However, this discussion does demonstrate that although the magnitude of the hydrodynamic pressure gradients is significantly smaller than the buoyancy, their effects should be accounted for due to their distinctly different impact on the flow. In the case of a vortex, even at low void fractions, bubbles spiralling around the core cause a reduction in the core diameter and as a result, an increase in vorticity.

When the bubbles reach their final location the direction of the force due to hydrodynamic pressure gradients becomes steady and as a result simply displaces the local fluid. This phase does not occur in the case of figure 14, since the vortex deformation results in bubble escape. However, in other cases, such as when there are fewer bubbles and less vortex deformation, a steady motion at the final location has been observed (e.g. see figure 13). In this case the hydrodynamic pressure gradients oppose the effect of gravity and cause a horizontal force against the direction of vortex ring motion. In the present conditions the downward force is small, only 14% of the gravity (accounting for the angle), and the gravity dominates the vertical distortion.

### 4.3. *Computation of bubble trajectories*

As noted in the previous subsection, one needs to determine the bubble trajectory in order to estimate its effect on the surrounding flow. In this subsection we demonstrate that by using the lift coefficients shown in figure 1(*b*), drag coefficients on a solid sphere, neglecting the Basset force (see the justification in Sridhar & Katz 1995) and using a virtual mass coefficient of 0.5, it is possible to estimate the bubble trajectory even in the present complex flow. The results are compared to the measured bubble trajectories.

We use the flow field whose vorticity distributions are shown in figure 14(*a–g*). The mean circulation is $160\,\mathrm{cm^2\,s^{-1}}$, the convection speed of the ring is $10.4\,\mathrm{cm\,s^{-1}}$. There are five 512 μm diameter bubbles, whose initial locations are obtained from the experimental data. The bubble trajectories are determined by solving the equation of motion for each bubble (equation (1*a*, *b*)) using a fourth-order Runge–Kutta method. The drag coefficient is determined using a Reynolds number based on the instantaneous relative velocity (Clift, Grace & Weber 1978), and the lift coefficient is estimated using the local vorticity (although it is a weak function of the vorticity). The velocity field within the vortex ring and the unsteady term in the equation, $\partial \boldsymbol{U}_l/\partial t$, are computed from PIV data measured at four discrete time steps (0, 97, 287, and 477 ms). Linear interpolation and second-order finite difference schemes are used for calculating velocities, spatial gradients and vorticities at intermediate time steps. The time steps are 1 ms.

The calculated trajectories of the entrained bubbles are plotted in figure 18(*a–e*) along with the experimental bubble locations on the four available images. As is evident from the plots, the predicted trajectories and entrainment times match the experimental data reasonably well, though there is some discrepancy in the trajectory of the fourth bubble (figure 18*d*). Here a discrepancy at an early stage caused the bubble to be transported in a substantially different direction. Note that this bubble

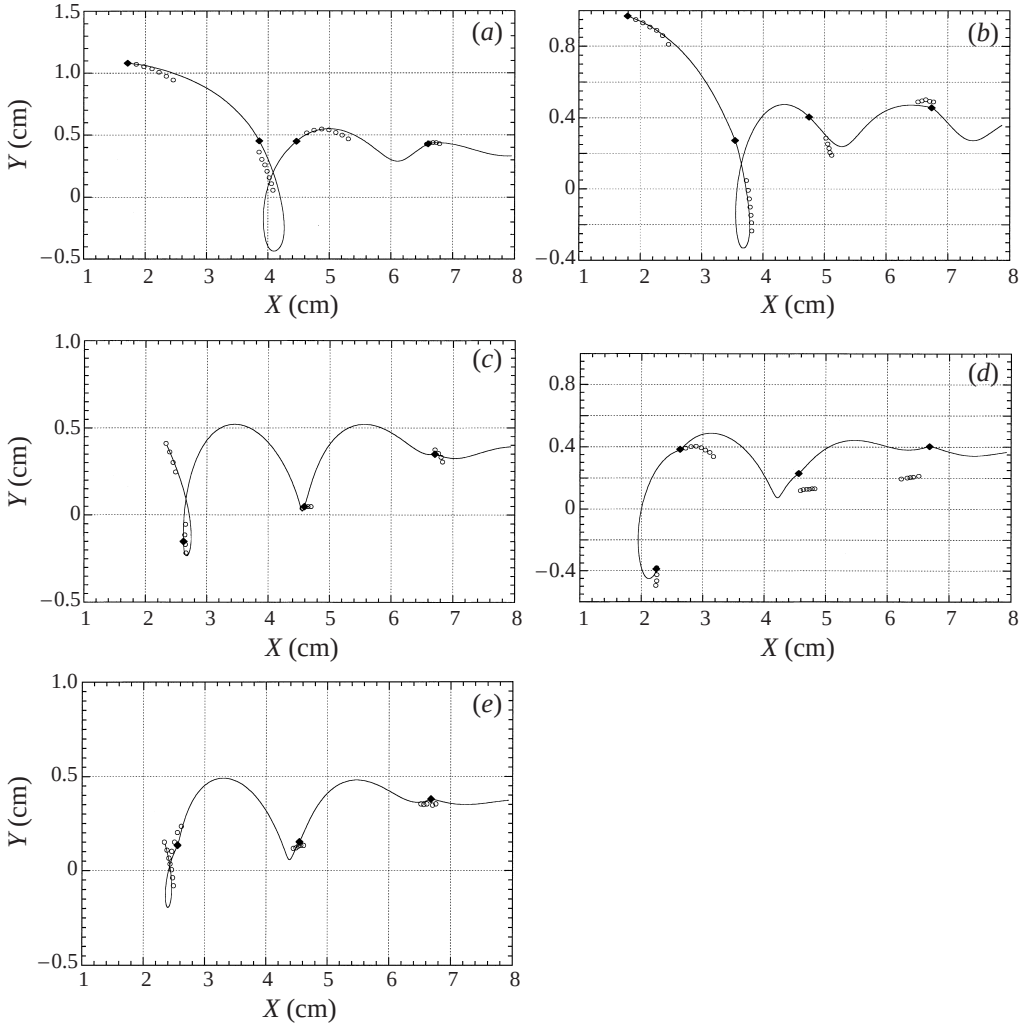


FIGURE 18. Comparisons between the measured and computed trajectories of the bubbles in figure 14. Solid line: computed trajectories obtained by integration of equation (1*a*, *b*). Open circles: the measured locations of the corresponding bubbles obtained from the PIV images. The experimental positions of each bubble are available at four time intervals starting at 0, 97, 287 and 477 ms. Within each interval, the four bubble positions are separated by 3.3 ms. Diamonds: computed location at the same instant as the first circle in each time interval. (*a–e*) Bubbles 1–5.

is also located 'far' from the other bubbles even after the entrainment into the core. In general however, the solution to equation (1*a*) using lift and drag coefficients measured in an undeformed vortex, can clearly predict the bubble trajectory even when the vortex is deformed. One should be careful, however, in drawing conclusions from these results. When the local shear forces and pressure gradients are sufficiently large to cause bubble deformation (unlike the present case, for which the characteristic Eötvös number is 0.086), one should expect to find significant variations in the magnitudes of the lift and drag coefficients. For example, a recent DNS analysis of large bubbles rising in a vertical shear flow (Ervin & Tryggvason 1997) has demonstrated that when bubble deformation becomes significant, the lift coefficient becomes negative.

## 5. Summary and conclusions

The influence of entrained microscopic bubbles on the strength and structure of a vortex is measured using cinematic PIV. It is demonstrated that for certain combinations of vortex strengths and bubble diameters, a few microscopic bubbles, at very low overall void fraction, shift and macroscopically deform the structure of the vortex. For example, five 512 μm diameter bubbles, entrained by a vortex with core diameter of 2 cm and strength of 160 $cm^2\,s^{-1}$, displace the core by 3.5 mm (35% of core radius and seven times the bubble diameter) and fragment the core into two regions with peak vorticities that are 20% higher than the original maximum vorticity. The total strength of the ring remains unchanged. When the bubbles escape from the vortex (in the present case they move along the centre of the ring to its upper side), the core returns to its original circular shape and location. The same phenomenon is observed with laminar, transitional and turbulent vortices. Thus, the process described here is clearly caused by the bubbles and is not related to ring stability.

Dimensional analysis along with the experimental data show that the distortion is maximum when the bubbles settle, following entrainment by the vortex (final location), in a region located between 20% to 40% of core radius. Smaller bubbles, that settle closer to the centre, do not affect the liquid momentum significantly, while larger bubbles are located too far from the core to distort it. $ga^3/\Gamma^2$ is identified as the non-dimensional parameter governing the 'final' bubble location in the present conditions (constant core radius). In general cases one should also take account of the core size, using parameters such as $gR^3/\Gamma^2$ or $a/R$. The effect of the ring Reynolds number, $\Gamma/v$, is small in the current range of flow conditions.

The vortex distortions are explained in terms of changes to the liquid momentum caused by the entrainment of the bubbles. In Appendix A it is argued and proven that the change to the liquid momentum due to the presence of the bubble is equal to the bubble volume multiplied by the local stresses that exist in the absence of the bubble. These stresses include gravity-induced (buoyancy) and hydrodynamic pressure gradients as well as viscous stresses. Both the buoyancy and the hydrodynamic pressure gradients have a significant impact on the structure of the vortex core, but their effects are distinctly different. During the stage when the bubbles spiral around the core the buoyancy translates the core vertically, while the hydrodynamic pressure gradients 'squeeze' it causing out-of-plane motion (continuity). Consequently, the core vorticity should increase. Estimated distortions agree with the experimental data. When the bubbles reach their final location, a phase that does not occur when the vortex is severely distorted, the direction of the force due to hydrodynamic pressure gradients becomes steady and as a result it simply displaces the local fluid.

This project was sponsored by the Office of Naval Research under grant number N00014-91-J-1176. The program manager is E. Rood. The authors would also like to gratefully acknowledge the numerous suggestions of and discussions with Omar Knio, Charles Meneveau and Andrea Prosperetti. Thanks are also due to the reviewers of this manuscript that led to substantial improvements and corrections.

## Appendix A. Modification of the liquid momentum due to the presence of a bubble

The momentum equation for a control volume with moving boundaries (Panton 1996) is

$$\frac{\mathrm{d}}{\mathrm{d}t}\int_{cv}\rho U_i\,\mathrm{d}V = \sum F_i - \int_{cs}\rho U_i(U_j - w_j)n_j\,\mathrm{d}s, \tag{A 1}$$

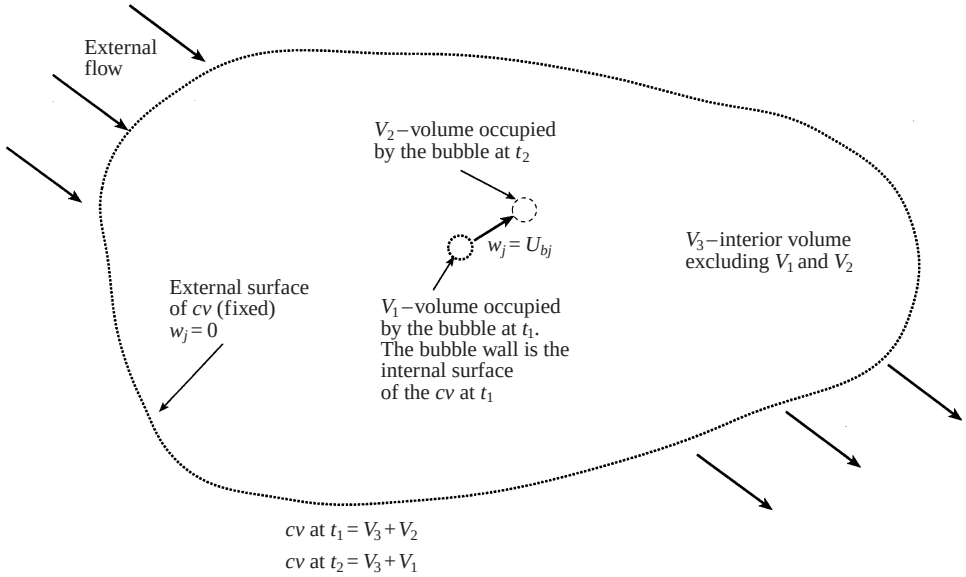


FIGURE 19. The control volume (CV) discussed in Appendix A.

where $U_i$ is the liquid velocity, $w_i$ is the velocity of the boundary of the control volume (*cv*) surrounded by a surface (*cs*), and $F_i$ is a force acting on this volume. Let us choose a control volume with fixed external boundaries that contains a single bubble, i.e. it has moving internal boundaries and fixed external boundaries (figure 19). For the purpose of the present discussion, we shall treat the bubble as a massless sphere. On the bubble wall the normal components of the liquid velocity and the bubble velocity are equal. Thus,

$$\int_{S_B} \rho U_i (U_j - w_j) n_j \, \mathrm{d}s = 0, \tag{A 2}$$

where $S_B$ is the bubble surface. On the external boundary $w_i = 0$. Thus,

$$\int_{S_E} \rho U_i (U_j - w_j) n_j \, \mathrm{d}s = \int_{S_E} \rho U_i U_j n_j \, \mathrm{d}s,$$

where $S_E$ is the external surface. Then, (A 1) becomes

$$\frac{\mathrm{d}}{\mathrm{d}t} \int_{cv} \rho U_i \, \mathrm{d}V = \sum F_i - \int_{S_E} \rho U_i U_j n_j \, \mathrm{d}s. \tag{A 3}$$

Also, based on the Leibnitz theorem (Panton 1996)

$$\begin{aligned} \frac{\mathrm{d}}{\mathrm{d}t} \int_{cv} \rho U_i \, \mathrm{d}V &= \int_{cv} \frac{\partial}{\partial t} \rho U_i \, \mathrm{d}V + \int_{cs} \rho U_i w_j n_j \, \mathrm{d}s \\ &= \int_{cv} \frac{\partial}{\partial t} \rho U_i \, \mathrm{d}V + \int_{S_E} \rho U_i w_j n_j \, \mathrm{d}s + \int_{S_B} \rho U_i w_j n_j \, \mathrm{d}s. \end{aligned} \tag{A 4}$$

On the external boundary $w_i = 0$. However, the integral on the bubble surface is not necessarily zero, unless one assumes a no-slip condition ($U_i = w_i$). This assumption is consistent with the drag being equal to that of a solid sphere. For $U_i = w_i$ on the

bubble surface, i.e. a constant $U_i = U_{bi}$,

$$\int_{S_B} \rho U_i w_j n_j \, \mathrm{d}s = \rho (U_b)_i \int_{S_B} (U_b)_j n_j \, \mathrm{d}s = 0.$$

Thus, (A 4) is reduced to

$$\frac{\mathrm{d}}{\mathrm{d}t} \int_{cv} \rho U_i \, \mathrm{d}V = \int_{cv} \frac{\partial}{\partial t} \rho U_i \, \mathrm{d}V. \tag{A 5}$$

Combining (A 5) with (A 3) gives

$$\int_{cv} \frac{\partial}{\partial t} \rho U_i \, \mathrm{d}V = \sum F_i - \int_{S_E} \rho U_i U_j n_j \, \mathrm{d}s. \tag{A 6}$$

The force term can be expressed as

$$\sum F_i = \int_{S_E} (-p n_i + \sigma_{ij} n_j) \, \mathrm{d}s + \int_{S_B} (-p n_i + \sigma_{ij} n_j) \, \mathrm{d}s + \int_{V_T} \rho g_i \, \mathrm{d}V - \int_{V_B} \rho g_i \, \mathrm{d}V, \tag{A 7}$$

where $V_T$ is the total volume and $V_B$ is the bubble volume. Since the mass of the bubble is assumed to be zero, the sum of the surface forces on the bubble is also zero, thus

$$\int_{S_B} (-p n_i + \sigma_{ij} n_j) \, \mathrm{d}s = 0. \tag{A 8}$$

The remaining equation is

$$\int_{cv} \frac{\partial}{\partial t} \rho U_i \, \mathrm{d}V + \int_{S_E} \rho U_i U_j n_j \, \mathrm{d}s = \int_{S_E} (-p n_i + \sigma_{ij} n_j) \, \mathrm{d}s + \int_{V_T} \rho g_i \mathrm{d}V - \int_{V_B} \rho g_i \, \mathrm{d}V. \tag{A 9}$$

This equation is different from that of a liquid flow without a bubble in two terms: the buoyancy force on the bubble (last term) and the boundary of integration in the first term (the bubble moves). The remaining issue is whether the displacement of a bubble affects the liquid momentum and to what extent. *We intend to show that the displacement of a small bubble alters the liquid momentum by an amount equal to the sum of the buoyancy force and the local liquid acceleration in the absence of the bubble multiplied by the bubble volume and the liquid density*. To prove this statement we assume that the bubble volume is substantially smaller than the control volume and as a result the boundary conditions are unaffected by the presence of the bubble (a discussion follows). At time $t_1$ the bubble is located at $\boldsymbol{x}_1$ (bold letters imply a vector) and occupies the volume $V_1$. At $t_2 > t_1$, the bubble is located at $\boldsymbol{x}_2$ and occupies $V_2$. We assume that $V_1 = V_2$. The rest of the control volume (excluding $V_1$ and $V_2$) is $V_3$. Aside from the displacement of the bubble there is no external unsteady forcing. Also, we define the mean liquid velocity within $V_1$ and $V_2$ (when they contain liquid) according to

$$\int_{V_2 \,\mathrm{at}\, t_1} \rho U_i \, \mathrm{d}V = \rho V_B \tilde{U}_i(\boldsymbol{x}_2, t_1), \quad \int_{V_1 \,\mathrm{at}\, t_2} \rho U_i \, \mathrm{d}V = \rho V_B \tilde{U}_i(\boldsymbol{x}_1, t_2), \tag{A 10}$$

where $V_B$ is the (small) bubble volume and the tilde indicates an average over the volume. The velocity field is divided into a flow that would exist in the absence of the bubble, $U_-^0$, and the (small) perturbation to this flow field caused by the presence of the bubble, $\Delta U^b$:

$$U_i = U_i^0 + \Delta U_i^b. \tag{A 11}$$

In a small time step $t_2 - t_1$ the change in momentum within the control volume is

$$\Delta \int_{cv} \rho U_i \, \mathrm{d}V = \int_{cv \text{ at } t_2} \rho U_i \, \mathrm{d}V - \int_{cv \text{ at } t_1} \rho U_i \, \mathrm{d}V$$
$$= \int_{V_1 \text{ at } t_2} \rho U_i \, \mathrm{d}V + \int_{V_3 \text{ at } t_2} \rho U_i \, \mathrm{d}V - \int_{V_2 \text{ at } t_1} \rho U_i \, \mathrm{d}V - \int_{V_3 \text{ at } t_1} \rho U_i \, \mathrm{d}V. \quad \text{(A 12)}$$

Using (A 11)

$$\Delta \int_{cv} \rho U_i \, \mathrm{d}V = \int_{V_3 \text{ at } t_2} \rho (U_i^0 + \Delta U_i^b) \, \mathrm{d}V - \int_{V_3 \text{ at } t_1} \rho (U_i^0 + \Delta U_i^b) \, \mathrm{d}V + \rho V_B$$
$$\times \left[ \tilde{U}_i^0(\boldsymbol{x}_1, t_2) + \Delta \tilde{U}_i^b(\boldsymbol{x}_1, t_2) \right] - \rho V_B \left[ \tilde{U}_i^0(\boldsymbol{x}_2, t_1) + \Delta \tilde{U}_i^b(\boldsymbol{x}_2, t_1) \right]. \quad \text{(A 13)}$$

For a small displacement

$$\tilde{U}_i^0(\boldsymbol{x}_2, t_1) = \tilde{U}_i^0(\boldsymbol{x}_1, t_2) + \frac{\partial \tilde{U}_i^0}{\partial x_j}(x_{2j} - x_{1j}) - \frac{\partial \tilde{U}_i^0}{\partial t} \Delta t, \quad \text{(A 14)}$$

$$\Delta \tilde{U}_i^b(\boldsymbol{x}_2, t_1) = \Delta \tilde{U}_i^b(\boldsymbol{x}_1, t_2) + \frac{\partial \Delta \tilde{U}_i^b}{\partial x_j}(x_{2j} - x_{1j}) - \frac{\partial \Delta \tilde{U}_i^b}{\partial t} \Delta t. \quad \text{(A 15)}$$

Thus,

$$\Delta \int_{cv} \rho U_i \, \mathrm{d}V = \int_{V_3 \text{ at } t_2} \rho (U_i^0 + \Delta U_i^b) \, \mathrm{d}V - \int_{V_3 \text{ at } t_1} \rho (U_i^0 + \Delta U_i^b) \, \mathrm{d}V - \rho V_B$$
$$\times \left[ \frac{\partial \tilde{U}_i^0}{\partial x} + \frac{\partial \Delta \tilde{U}_i^b}{\partial x} \right] (x_{2j} - x_{1j}) + \rho V_B \left[ \frac{\partial \tilde{U}_i^0}{\partial t} + \frac{\partial \Delta \tilde{U}_i^b}{\partial t} \right] \Delta t. \quad \text{(A 16)}$$

As $\Delta t \to 0$

$$\int_{cv} \frac{\partial}{\partial t} \rho U_i \, \mathrm{d}V = \int_{V_3} \frac{\partial}{\partial t} \rho U_i^0 \, \mathrm{d}V + \int_{V_3} \frac{\partial}{\partial t} \rho \Delta U_i^b \, \mathrm{d}V$$
$$+ \rho V_B \left( \frac{\partial \tilde{U}_i^0}{\partial t} + \frac{\partial \Delta \tilde{U}_i^b}{\partial t} \right) - \rho V_B \left[ \frac{\partial \tilde{U}_i^0}{\partial x_j} + \frac{\partial \Delta \tilde{U}_i^b}{\partial x_j} \right] U_{bj}, \quad \text{(A 17)}$$

where $U_b$ is the bubble velocity which is equal to the local liquid velocity due to no slip. Based on the assumption that the bubble does not alter the boundary conditions compared to a flow without a bubble

$$\int_{V_1+V_2+V_3} \frac{\partial}{\partial t} \rho U_i^0 \, \mathrm{d}V = - \int_{S_E} \rho U_i U_j n_j \, \mathrm{d}s + \int_{S_E} (-p n_i + \sigma_{ij} n_j) \, \mathrm{d}s + \int_{V_T} \rho g_i \, \mathrm{d}V. \quad \text{(A 18)}$$

And using (A 9)

$$\int_{V_1+V_2+V_3} \frac{\partial}{\partial t} \rho U_i^0 \, \mathrm{d}V = \int_{cv} \frac{\partial}{\partial t} \rho U_i \, \mathrm{d}V + \int_{V_B} \rho g_i \, \mathrm{d}V. \quad \text{(A 19)}$$

Substituting in (A 17)

$$\int_{V_1+V_2+V_3} \frac{\partial}{\partial t} \rho U_i^0 \, \mathrm{d}V - \int_{V_B} \rho g_i \, \mathrm{d}V$$
$$= \int_{V_3} \frac{\partial}{\partial t} \rho U_i^0 \, \mathrm{d}V + \int_{V_3} \frac{\partial}{\partial t} \rho \Delta U_i^b \, \mathrm{d}V + \rho V_B \left( \frac{\partial \tilde{U}_i^0}{\partial t} + \frac{\partial \Delta \tilde{U}_i^b}{\partial t} \right)$$
$$- \rho V_B \left[ \frac{\partial \tilde{U}_i^0}{\partial x_j} + \frac{\partial \Delta \tilde{U}_i^b}{\partial x_j} \right] U_j. \quad \text{(A 20)}$$

Since for a short displacement

$$\int_{V_2} \frac{\partial}{\partial t}\rho U_i^0 \,\mathrm{d}V \approx \int_{V_1} \frac{\partial}{\partial t}\rho U_i^0 \,\mathrm{d}V \approx \rho V_B \left(\frac{\partial \tilde{U}_i^0}{\partial t}\right), \tag{A 21}$$

(A 20) then becomes

$$\rho V_B \left[\frac{\partial \tilde{U}_i^0}{\partial t} + \left(\frac{\partial \tilde{U}_i^0}{\partial x_j} + \frac{\partial \Delta \tilde{U}_i^b}{\partial x_j}\right)(U_j^0 + \Delta U_j^b)\right] - \int_{V_B} \rho g_i \,\mathrm{d}V$$
$$= \int_{V_3} \frac{\partial}{\partial t}\rho \Delta U_i^b \,\mathrm{d}V + \rho V_B \left(\frac{\partial \Delta \tilde{U}_i^b}{\partial t}\right). \tag{A 22}$$

The right-hand side involves integration of $\partial \Delta U_i^b/\partial t$ over the entire liquid within the control volume ($V_3$ and one bubble volume form the entire $cv$, although the second term is of a higher order since $V_B$ is small). On the left-hand side $\partial \Delta U_i^b/\partial x_-$ is small compared to $\partial U_i^0/\partial x_-$. Keeping only first-order terms

$$\rho V_B \left[\frac{\mathrm{D}\tilde{U}_i^0}{\mathrm{D}t} - g_i\right] = \int_{cv} \frac{\partial}{\partial t}\rho \Delta U_i^b \,\mathrm{d}V = \Delta F_i^b, \tag{A 23}$$

where D indicates material derivative. Equation (A 23) shows that displacement of a bubble in an unsteady and non-uniform flow field alters the momentum of the remaining liquid in the control volume (denoted as $\Delta F_i^b$). This result brings into question the validity of assuming steady boundary conditions (both stresses and momentum flux). If the velocity within the control volume changes, it should affect the conditions at the boundary. Furthermore, a bubble in a flow field for which $\partial p/\partial x_i \neq 0$ deforms and changes its volume. Thus, the exact solution to this problem is complex and is beyond the scope of the present discussion.

Note that during infinitesimal bubble displacement $V_1$ and $V_2$ overlap and as a result there is a potential problem with the validity of (A 10). However, this issue has no impact on the final results. To illustrate this point, suppose $V_1$ and $V_2$ overlap and the joint volume is $V_j$. Thus, the boundaries on the right-hand side of (A 12) would change to

$$\Delta \int_{cv} \rho U_i \,\mathrm{d}V = \int_{cv \text{ at } t_2} \rho U_i \,\mathrm{d}V - \int_{cv \text{ at } t_1} \rho U_i \,\mathrm{d}V$$
$$= \int_{V_1 - V_j \text{ at } t_2} \rho U_i \,\mathrm{d}V + \int_{V_3 \text{ at } t_2} \rho U_i \,\mathrm{d}V - \int_{V_2 - V_j \text{ at } t_1} \rho U_i \,\mathrm{d}V - \int_{V_3 \text{ at } t_1} \rho U_i \,\mathrm{d}V,$$

namely the integration is performed only on the portion that contains liquid. Using the same simplification introduced in (A 10), and going through the same steps would add the term $-\rho V_j \partial \tilde{U}_i/\partial t$ to the right-hand side of (A 17) and (A 20). However, the overlap also changes the boundary of the integral on the left-hand side of (A 18)–(A 20) to $V_3 + V_1 + V_2 - V_j$, resulting in an additional term $-\int_{V_j} \partial/\partial t(\rho U_i^0)\,\mathrm{d}v$ on the left-hand side. Within the present assumptions the new terms on both sides of (A 20) cancel each other resulting in the same answer.

Another approach introduced recently by Druzhinin & Elgobashi (1998) leads to the same conclusion. They also divide the flow field into $U_-^0$ and $\Delta U^b$. The corresponding

pressures are $p^0$ and $\Delta p^b$. The force acting on the surface of the bubble is then:

$$\int_{S_B}(-pn_i+\sigma_{ij}n_j)\,\mathrm{d}S=\int_{S_B}(-p^0n_i+\sigma^0_{ij}n_j)\,\mathrm{d}S+\int_{S_B}(-\Delta p^bn_i+\Delta\sigma^b_{ij}n_j)\,\mathrm{d}S$$
$$=F^0_i+(-\Delta F^b_i)=0. \tag{A 24}$$

Here $n_i$ is pointing to the liquid and $F^0_i$ and $-\Delta F^b_i$ are the results of the first and second integrals, respectively. $F^0_i$ can be determined from the Navier–Stokes equation for a flow field without a bubble. Assuming a small bubble

$$F^0_i=\left[-\frac{\partial p^0}{\partial x_i}+\frac{\mu\partial^2\tilde{U}^0_i}{\partial x_j\partial x_j}\right]V_B=\left[\rho\left(\frac{\mathrm{D}\tilde{U}^0_i}{\mathrm{D}t}-g_i\right)\right]V_B. \tag{A 25}$$

Druzhinin & Elgobashi (1998) argue (and we agree) that $-\Delta F^b_i$ is the change to the total force acting on the bubble resulting from the modifications to the flow field due to the presence of the bubble. Thus, $\Delta F^b_i$ represents an additional force acting on the liquid. Note that to determine $\Delta F^b_i$ one needs to solve the following equation:

$$-\frac{\partial\Delta p^b}{\partial x_i}+\frac{\mu\partial^2\Delta U^b_i}{\partial x_j\partial x_j}=\rho\left(\frac{\partial\Delta U^b_i}{\partial t}+U^0_j\frac{\partial\Delta U^b_i}{\partial x_j}+\Delta U^b_j\frac{\partial(U^0_i+\Delta U^b_i)}{\partial x_j}\right). \tag{A 26}$$

This expression is obtained by subtracting the Navier–Stokes equation for $U^0_i$ from the equation for $U_i$. Since for a bubble $\Delta F^b_i=F^0_i$, we obtain the same result as before.

Let us examine the implication of the result in (A 23) for several relevant simple flows:

(i) A bubble rising in an otherwise stagnant fluid with gravity. Here $U^0_i=0$ and as a result the force applied by the bubble on the liquid is equal to the buoyancy force.

(ii) A bubble in a free falling liquid. Here

$$\frac{\mathrm{D}U^0_i}{\mathrm{D}t}=g_i,\qquad \Delta F^b_i=0. \tag{A 27}$$

(iii) A bubble moving in a horizontal nozzle that would have a steady flow in the absence of the bubble and with no gravity. Here

$$\Delta F^b_i=\rho V_B\left[\frac{\mathrm{D}\tilde{U}^0_i}{\mathrm{D}t}\right]=\rho V_B\tilde{U}^0_1\frac{\partial\tilde{U}^0_1}{\partial x}. \tag{A 28}$$

To understand this result note that based on (A 9) the total momentum within the control volume remains constant (assuming steady outer boundary conditions). However, as the bubble moves it occupies volumes that in its absence would have different velocities. Thus, to maintain an overall constant momentum the velocity of the liquid in the rest of the control volume must adjust by an amount equal to the rate of change in the liquid momentum displaced by the bubble.

(iv) A bubble located at $r$ in a vortex with strength $\Gamma$, core radius $R$, uniform vorticity distribution and without gravity. Here

$$|\Delta F^b|=\rho V_B\Gamma^2r/4\pi^2R^4 \tag{A 29}$$

and the direction is towards the centre of the vortex. As discussed in the main text, when several bubbles surround the core during entrainment they cause a reduction in the core size and an increase in the core vorticity.

(v) In a general case, as discussed in the text, the stresses associated with the undisturbed flow (hydrodynamic and due to gravity) are balanced by the lift, drag,

virtual mass and Bassett forces. Neglecting the latter and using (1*a*)

$$\Delta \boldsymbol{F}^b = \rho V_B \left( \frac{\mathrm{D}\boldsymbol{U}^0}{\mathrm{D}t} - \boldsymbol{g} \right)$$

$$= -\rho V_B \left[ \frac{3}{8a} C_d |\boldsymbol{U}_{rel}| \boldsymbol{U}_{rel} + \frac{3}{8a} C_l |\boldsymbol{U}_{rel}|^2 \frac{\boldsymbol{U}_{rel} \times \boldsymbol{\omega}}{|\boldsymbol{U}_{rel}||\boldsymbol{\omega}|} - \frac{1}{2} \left( \frac{\mathrm{D}\boldsymbol{U}_b}{\mathrm{D}t} - \frac{\mathrm{D}\boldsymbol{U}^0}{\mathrm{D}t} \right) \right] \quad \text{(A 30)}$$

where bold letters indicate a vector and $\boldsymbol{U}_{rel} = \boldsymbol{U} - \boldsymbol{U}_b$.

## Appendix B. Uncertainty in velocity measurements – PIV

The accuracy of the PIV measurement depends on image quality (distortion, signal to noise ratio, etc.), magnification, window and particle image sizes, the number of particle pairs per window, the method used for interpolating the correlation data in order to get sub-pixel accuracy, etc. The overall accuracy of the present procedure was studied by Dong *et al.* (1992) and Roth *et al.* (1995). They show that the error level decreases with increasing number of particle pairs in the interrogation window. The improvement is doubled as the number of particle pairs is increased from one to four, after which the improvement is slower (15% decrease when concentration is increased to eight pairs). The uncertainty is also affected by image magnification. In general, as the magnification is increased while keeping the number of particle pairs the same, the accuracy of the technique also increases. The limiting factors are the resolution limits of the film and lenses. In the present experiment the mean displacements are typically around 40 pixels, and there are at least four particle pairs in each interrogation window. Since the characteristic uncertainty in displacement is 0.4 pixels, the corresponding error in velocity is slightly less than 1%. The relative error in vorticity measurement is less than 10%.

### B.1. *Uncertainty in particle tracking measurements*

The uncertainty in velocity measurements using 'particle tracking' is due to errors in measuring the particle displacements, as well to errors associated with interpolation (Sridhar & Katz 1995). As noted before, individual particle displacements are determined by correlating between their corresponding particle traces. Enhanced sub-pixel accuracy is achieved by fitting a curve to the correlation function and computing the peak of the fitted function. Repeated examinations of randomly selected traces show that uncertainty in measured particle displacements in 0.4 pixels. This value is conservative since it represents the maximum deviation between results. The corresponding error in the fluid velocity at a grid point, which is determined by interpolation, ranges from 0.23 to 0.29 pixels/(laser pulse interval). Thus, by selecting a magnification of 1300 pixels $\mathrm{cm}^{-1}$, with typical particle displacement range between 80 and 120 pixels, it is possible to maintain a relative error in particle tracking measurement of 0.25% to 0.35%. There are other sources of error as outlined below due to temporal averaging and bilinear interpolation.

### B.2. *Temporal averaging error*

This error occurs as a result of assuming a straight-line trajectory between traces of an individual particle. To quantify this error, the velocity field is modelled as a thin tube vortex ring, which is described by Batchelor (1967). Selecting a particular site, the location of a particle at three instants is computed using the theoretical flow field. The corresponding particle velocity is estimated from its discrete locations

and compared to the actual mean value. As expected, the error in estimating the velocity from the particle displacement increases with the delay between pulses and with decreasing distance from the vortex centre. However, for all the data presented in this paper, the temporal averaging error in velocity is less than 0.1%.

### B.3. *Interpolation error*

Using the same vortex model, the accuracy of the velocity data obtained from neighbouring particle traces is also estimated. The velocity and accelerations at four points, located around the site of interest, is first determined. The present interpolation scheme is then used to estimate the velocity and acceleration at the desired site and compared to the exact values. We can now determine the overall uncertainties in the velocity and vorticity due to measurement, temporal averaging and spatial interpolation errors. The typical uncertainty in the fluid velocity is less than 0.9% while the relative error in the vorticity is less than 10%.

## REFERENCES


Adrian, R. J. 1991 Particle-imaging techniques for experimental fluid mechanics. *Ann. Rev. Fluid Mech.* **23**, 261.

Auton, T. R., Hunt, J. C. R. & Prud'homme, M. 1988 The force exerted on a body in inviscid unsteady non-uniform rotational flow. *J. Fluid Mech.* **197**, 241.

Batchelor, G. K. 1967 *An Introduction to Fluid Dynamics*. Cambridge University Press.

Bessler, W. F. & Littman, H. 1987 Experimental studies of wakes behind circularly capped bubbles. *J. Fluid Mech.* **185**, 137.

Bhaga, B. & Weber, M. E. 1981 Bubbles in viscous liquids: Shapes, wakes and velocities. *J. Fluid Mech.* **105**, 61.

Clift, R., Grace, J. R. & Weber, M. E. 1978 *Bubbles, Drops and Particles*. Academic.

Crowe, C. T. 1991 The state-of-the-art in the development of numerical models for dispersed phase flows. *Proc. Intl Conf. on Multiphase Flows, Tsukuba*, 49.

Dandy, D. S. & Dwyer, H. A. 1990 A sphere in a shear flow at finite Reynolds number: effect of shear on particle lift, drag, and heat transfer. *J. Fluid Mech.* **216**, 381.

Didden, N. 1979 On the formation of vortex rings: Rolling up and production and circulation. *Z. Angew. Math. Phys.* **30**, 101.

Dong, R., Chu, S. & Katz, J. 1992 Quantitative visualization of the flow within the volute of a centrifugal pump. Part A: Technique. *Trans. ASME J. Fluids Engng* **114**, 390.

Druzhinin, O. A. & Elgobashi, S. 1998 Direct numerical simulations of bubble-laden turbulent flows using the two fluid formulation. *Phys. Fluids* **10**, 685–697.

Eaton, J. K. 1994 Experiments and simulations of turbulence modification by dispersed particles. *Appl. Mech. Rev.* **46**, S44.

Elghobashi, S. & Truesdell, G. C. 1993 On the two-way interaction between homogeneous turbulence and dispersed solid particles. I: Turbulence modification. *Phys. Fluids* A **5**, 1790.

Ervin, E. A. & Tryggvason, G. 1997 The rise of bubbles in a vertical shear flow. *Trans. ASME J. Fluids Engng* **119**, 443.

Fan, L. S. & Tsuchiya, K. 1990 *Bubble Wake Dynamics in Liquids and Liquid-Solid Suspensions*. Butterworth-Heinemann.

Fleckhaus, D., Hishida, K. & Maeda, M. 1987 Effect of laden solid particles on the turbulent flow structure of a round free jet. *Exps. Fluids* **5**, 323.

Glezer, A. 1988 On the formation of vortex rings. *Phys. Fluids* **31**, 3532.

Gore, R. A. & Crowe, C. T. 1989 Effect of particle size on modulating turbulence intensity. *Intl J. Multiphase Flow* **15**, 279.

Hetsroni, G. 1993 The effect of particles on the turbulence in a boundary layer. In *Particulate Two-Phase Flow* (ed. M. C. Roco), p. 244. Butterworth–Heinemann.

Katz, J. & Meneveau, C. 1996 Wake induced relative motion of bubbles rising in line. *Intl J. Multiphase Flows* **22**, 239.

Loth, E. & Cybrinzski, M. S. 1994 Modulation of shear layer thickness due to large bubbles. *Intl J. Multiphase Flow* **21**, 919.

Maxey, M. R. & Riley, J. J. 1983 Equation of motion for a small rigid sphere in a nonuniform flow. *Phys. Fluids* **26**, 883.

Maxworthy, T. 1974 Turbulent vortex rings. *J. Fluid Mech.* **64**, 227.

Maxworthy, T. 1977 Some experimental studies of vortex rings. *J. Fluid Mech.* **81**, 465.

Naciri, M. A. 1992 Contribution à l'étude des forces exercées par un liquide sur une bulle de gaz: portance, masse ajoutée et interactions hydrodynamiques. PhD thesis, L'Ecole Centrale De Lyon, Lyons.

Panton, R. L. 1996 *Incompressible Flow*. John Wiley & Sons.

Ran, B. & Katz, J. 1991 The response of microscopic bubbles to sudden changes in the ambient pressure. *J. Fluid Mech.* **224**, 91.

Rightley, P. M. & Lasheras, J. C. 1995 Bubble dispersion and interphase coupling in a free shear layer. *Intl Mechanical Engineering Congress*, ASME, vol. 321, p. 461.

Roth, G., Hart, D. & Katz, J. 1995 Feasibility of using the L64720 Video Motion Estimation Processor (MEP) to increase effectiveness of velocity map generation using Particle Image Velocimetry (PIV). *Laser Anemometry*. ASME FFD, vol. 229, p. 387.

Rubinov, S. I. & Keller, J. B. 1991 The transverse force on a spinning sphere moving in a viscous fluid. *J. Fluid Mech.* **11**, 447.

Ruetsch, G. R. & Meiburg, E. 1994 Two-way coupling in shear layers with dilute bubble concentrations. *Phys. Fluids* **6**, 2656.

Saffman, P. G. 1965 The lift on a small sphere in a slow shear flow. *J. Fluid Mech.* **22**, 385 and Corrigendum, *J. Fluid Mech.* **31**, 624 (1968).

Sallet, D. W. & Widmayer, R. S. 1974 An experimental investigation of laminar and turbulent vortex rings in air. *Z. Flugwiss* **22**, 207.

Sridhar, G. & Katz, J. 1995 Drag and lift forces on a bubble entrained by a vortex. *Phys. Fluids* **7**, 389.

Sridhar, G., Ran, B. & Katz, J. 1991 Implementation of particle image velocimetry to multiphase flows. *Cavitation and Multiphase Flow Forum* **109**, 205.

Taeibi-Rahni, M., Loth, E. & Tryggvason, G. 1994 Flow modulation of a planar free shear layer with large bubbles – Direct numerical simulations. *Intl J. Multiphase Flow* **20**, 1109.